

Quantitative analysis of a footwall-scarp degradation complex and syn-rift stratigraphic architecture, Exmouth Plateau, NW Shelf, offshore Australia

Bonita J. Barrett^{1,2}  | David M. Hodgson¹  | Christopher A.-L. Jackson³  |
Christopher Lloyd⁴  | Junia Casagrande¹ | Richard E. Ll. Collier¹ 

¹School of Earth and Environment, University of Leeds, Leeds, United Kingdom

²Equinor ASA, Equinor Research Centre, Ranheim, Norway

³Basin Research Group (BRG), Department of Earth Science & Engineering, Imperial College, London, United Kingdom

⁴School of Earth & Environmental Sciences, University of Manchester, Manchester, United Kingdom

Correspondence

Bonita J. Barrett, Equinor ASA, Equinor Research Centre, Arkitekt Ebbells veg 10, 7053, Ranheim, Norway.
Email: bonb@equinor.com

Abstract

Interactions between footwall-, hangingwall- and axial-derived depositional systems make syn-rift stratigraphic architecture difficult to predict, and preservation of net-erosional source landscapes is limited. Distinguishing between deposits derived from fault-scarp degradation (consequent systems) and those derived from long-lived catchments beyond the fault block crest (antecedent systems) is also challenging, but important for hydrocarbon reservoir prospecting. We undertake geometric and volumetric analysis of a fault-scarp degradation complex and adjacent hangingwall-fill associated with the Thebe-2 fault block on the Exmouth Plateau, NW Shelf, offshore Australia, using high resolution 3D seismic data. Vertical and headward erosion of the complex and fault throw are measured. Seismic-stratigraphic and seismic facies mapping allow us to constrain the spatial and architectural variability of depositional systems in the hangingwall. Footwall-derived systems interacted with hangingwall- and axial-derived systems, through diversion around topography, interfingering or successive onlap. We calculate the volume of footwall-sourced hangingwall fans (V_{HW}) for nine quadrants along the fault block, and compare this to the volume of material eroded from the immediately up-dip fault-scarp (V_{FW}). This analysis highlights areas of sediment bypass ($V_{FW} > V_{HW}$) and areas fed by sediment sources beyond the degraded fault scarp ($V_{HW} > V_{FW}$). Exposure of the border fault footwall and adjacent fault terraces produced small catchments located beyond the fault block crest that fed the hangingwall basin. One source persisted throughout the main syn-rift episode, and its location coincided with: (a) an intra-basin topographic high; (b) a local fault throw minimum; (c) increased vertical and headward erosion within the fault-scarp degradation complex; and (d) sustained clinoform development in the immediate hangingwall. Our novel quantitative volumetric approach to identify through-going sediment input points could be applied to other rift basin-fills. We highlight implications for hydrocarbon exploration and emphasize the need to incorporate interaction of multiple sediment sources and their resultant architecture in tectono-stratigraphic models for rift basins.

This is an open access article under the terms of the Creative Commons Attribution License, which permits use, distribution and reproduction in any medium, provided the original work is properly cited.

© 2020 The Authors. Basin Research published by International Association of Sedimentologists and European Association of Geoscientists and Engineers and John Wiley & Sons Ltd

1 | INTRODUCTION

Fault-scarp degradation (e.g. Bilal, McClay, & Scarselli, 2018; Elliott et al., 2012; Henstra et al., 2016; Leeder & Jackson, 1993; Morley, Ionnikoff, Pinyochon, & Seusutthiya, 2007; Mortimer & Carrapa, 2007; Underhill et al., 1997; Welbon et al., 2007) typically feeds sediment into its immediate hangingwall basin to form subaerial and subaqueous fans (Fraser & Robinson, 2002; Leeder et al., 2002; McLeod & Underhill, 1999; Sharp, Gawthorpe, Armstrong, & Underhill, 2000; Stewart & Reeds, 2003; Figure 1). In a simple source-to-sink configuration, the size of the related catchment (Bilal et al., 2018; Elliott et al., 2012; Leeder & Jackson, 1993; Nyberg et al., 2018), and the stratigraphic architecture of adjacent hangingwall fans relate to fault throw and climate (Barrett, Collier, et al., 2019; Barrett, Hodgson, Collier, & Dorrell, 2018; Dorsey & Umhoefer, 2000; Dorsey, Umhoefer, & Renne, 1995; Gawthorpe et al., 2017; Gawthorpe, Fraser, & Collier, 1994; Ghinassi, 2007). The few studies that attempt an integrated assessment of footwall degradation and hangingwall architecture are mainly from recently active systems (e.g. Alves & Cupkovic, 2018; Collier & Gawthorpe, 1995; Pechlivanidou et al., 2018), and lack 3D constraints.

Two principal sources supply material from the footwall to the hangingwall of a rift basin: (a) the immediate scarps of normal faults; i.e. consequent systems, and (b) through-going sediment inputs from established catchments located beyond the immediate fault block crest, i.e. antecedent systems (Figure 1; Gawthorpe & Leeder, 2000; Leeder & Gawthorpe, 1987). Differentiating between consequent

Highlights

- Integrated assessment of syn-rift footwall degradation and hangingwall-fill
- Unravelling interactions between different sediment sources recorded in hangingwall architecture
- Novel volume balancing approach to locate through-going footwall sediment input points
- Implications for syn-rift play potential on the Exmouth Plateau and analogous rift basin-fills

and antecedent supply signals in the rock record is difficult. First, in the absence of provenance, textural maturity, and biostratigraphic data, it is challenging to determine sediment source areas and the relative ages between syn-rift units. Second, many exposed active or inactive rifts lack fully three-dimensional exposure of hangingwall stratigraphy and the related footwall erosional landscapes. Third, subsurface imaging of drainage catchments is rare because of the limited preservation of such erosional landscapes (e.g. Elliott et al., 2012; Hartley, Roberts, White, & Richardson, 2011; Smallwood & Gill, 2002; Stucky de Quay, Roberts, Watson, & Jackson, 2017; Turner et al., 2018). The ability to discriminate between these two inputs is important for understanding sediment transport to and within the basin, and also for reservoir quality assessment of hangingwall fans (Leppard & Gawthorpe, 2006; Reading & Richards, 1994; Richards, Bowman, & Reading, 1998). We thus require a method for determining the location of

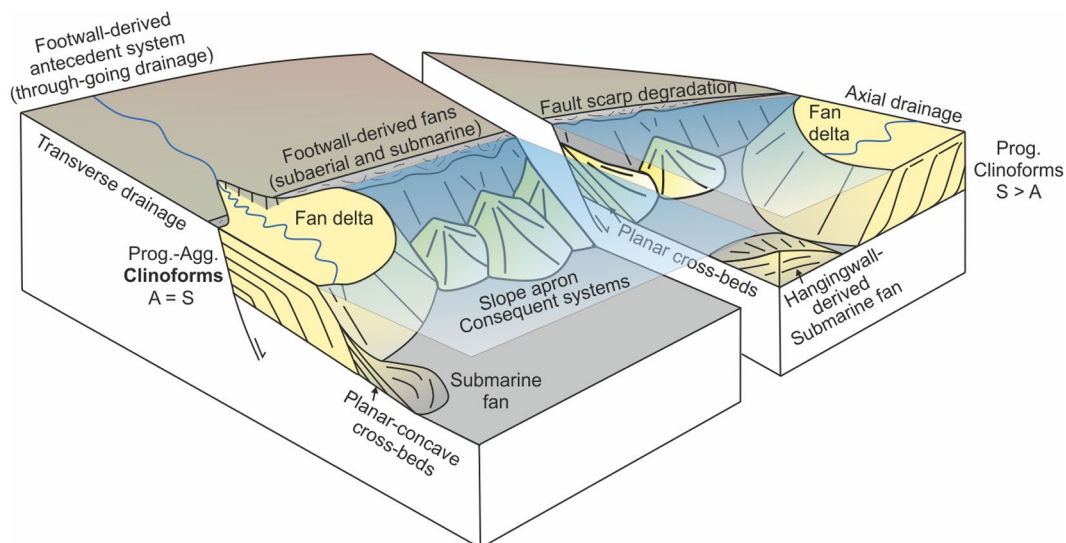


FIGURE 1 Conceptual tectono-sedimentary model of an individual fault block in the syn-rift phase. Footwall-, hangingwall- and axial-derived depositional systems are illustrated with their cross-sectional geometries, which may be apparent in seismic data. The difference between antecedent (through-going) and consequent drainage systems is highlighted. S = Sediment supply; A = Accommodation

through-going sediment input points from seismic data. Mass balancing is a common technique in large-scale source-to-sink studies (Hampson, Duller, Petter, Robinson, & Allen, 2014; Lin & Bhattacharya, 2017; Michael, Whittaker, & Allen, 2013; Paola & Martin, 2012; Watkins et al., 2018). Such a pragmatic approach could be used to decipher supply signals by constraining and understanding the origin of any volume deficits between hangingwall deposits and their up-dip footwall-hosted catchments. Only areal comparisons have been attempted so far (e.g. Chen, Wood, & Gawthorpe, 2020), but consideration of the eroded and deposited volume is necessary to accurately constrain the source-to-sink relationship.

Although, footwall-derived depositional systems are most commonly reported (e.g. Backert, Ford, & Malartre, 2010; Ford, Williams, Malartre, & Popescu, 2007; Gawthorpe et al., 1994; Leppard & Gawthorpe, 2006; Turner et al., 2018), in rifts defined by prominent pre-rift topography, and in which antithetic faults, folds, and interacting fault arrays are widespread, hangingwall- and axial-derived systems can be as influential as antecedent footwall-derived systems in controlling the basin infill (Figure 1; Jackson, Larsen, Hanslien, & Tjemsland, 2011; Leeder, Mack, & Salyards, 1996; McArthur, Hartley, Archer, Jolley, & Lawrence, 2016). How multiple depositional systems interact within a fault-confined basin, and how those interactions evolve with the growth of associated structural elements (e.g. secondary faults and folds), is relatively understudied (Jackson, Gawthorpe, & Sharp, 2006; Lewis, Jackson, & Gawthorpe, 2015; Serck & Braathen, 2019; Sharp, Gawthorpe, Underhill, & Gupta, 2000). A better understanding of these processes is necessary to unravel the complexity of the ultimate depositional architecture of a hangingwall basin-fill.

Here, we analyse footwall degradation and associated hangingwall-fill across an individual fault block (Thebe-2) on the Exmouth Plateau, northern Carnarvon Basin, NW Shelf, Australia. This is undertaken using high-quality 3D seismic reflection and well data, with a novel volume-balancing approach. Our aims are to: (a) assess the interaction between multiple depositional systems with different origins in a fault-confined basin and the influence of evolving rift structure on their development; (b) identify the position of footwall-derived, through-going sediment entry points in the absence of direct seismic imaging of the related catchment; (c) discuss the implications of the developed approach for hydrocarbon exploration; and (d) present a quantitatively-informed interpretation of the tectono-sedimentary evolution of the basin. This study can be used to inform studies of other hangingwall basins, where the coeval, net-erosional footwall system is poorly preserved, and emphasizes the need to incorporate multiple sediment sources and detailed interactions

between their deposits into tectono-stratigraphic models of rift basin-fills.

2 | STUDY AREA

The offshore, northern Carnarvon Basin (535 000 km²; Figure 2) is positioned towards the southern limit of the NW Shelf, Australia, and is bounded by the Argo, Gascoyne and Cuvier Abyssal Plains to the north, west and southwest, respectively (Hocking, Moors, & Van de Graaff, 1988). Internally, the basin comprises several NE-trending, Palaeozoic-Cenozoic structural elements that accommodate a <15 km thick sedimentary succession (Hocking et al., 1988). The Beagle, Dampier, Barrow and Exmouth sub-basins are located in the inboard region of the basin and represent failed rift systems (Gartrell, Torres, Dixon, & Keep, 2016; McHarg, Elders, & Cunneen, 2018; Stagg & Colwell, 1994; Figure 2a). The Exmouth Plateau is a bathymetric plateau that sits outboard of these sub-basins (Figure 2c). It is a broad 600 km long and 300–400 km wide, relatively undeformed platform that consists of stretched continental crust that is intersected by NNE-SSW-striking, domino-style extensional faults, which formed since the Late Triassic (Exon, Haq, & von Rad, 1992; Gartrell, 2010; Gartrell et al., 2016). Many of the faults are characterized by prominent fault-scarp degradation (Bilal et al., 2018). The footwall highs have been exploited for hydrocarbons, with the discovery in the Thebe-2 fault footwall, being one of the most basinward (c. 350 km offshore) on the Exmouth Plateau (Williams, 2018). The footwall of the NW-dipping Thebe-2 fault and its associated hangingwall basin are the focus of this study (Figure 2b,c). The Thebe-2 hangingwall basin is 16 km long and has a maximum width of 3.7 km. The Thebe-2 fault strikes NNE-SSW, bounds the basin to the east and has a maximum throw of 642 ms (424 m using a velocity of 2320 m/s). Four minor, SE-dipping, antithetic faults, which are sub-parallel to the main border fault, bound the sub-basin to the west.

The pre-rift succession across much of the Exmouth Plateau comprises Triassic fluvio-deltaic clastics (Mungaroo Formation). This formation is eroded at the crest of the Thebe-2 fault block, as well as at many other fault blocks across the Exmouth Plateau (Figure 3; Bilal et al., 2018). The base and top of the studied interval are defined by the Rhaetian TR30.1 transgressive surface (TS; 209.5 Ma) and the Oxfordian J40.0 sequence boundary (SB; 162.5 Ma), respectively (Marshall & Lang, 2013; Figure 3). Well data show that the TR30.1 TS - J40.0 SB sequence, inferred to be the Brigadier, Murat and Athol Formations, is condensed on the footwall of the fault (2–3 m) and below seismic resolution. Overlying the J40.0 SB and overlapping the degraded fault scarp is the Late Jurassic-Early

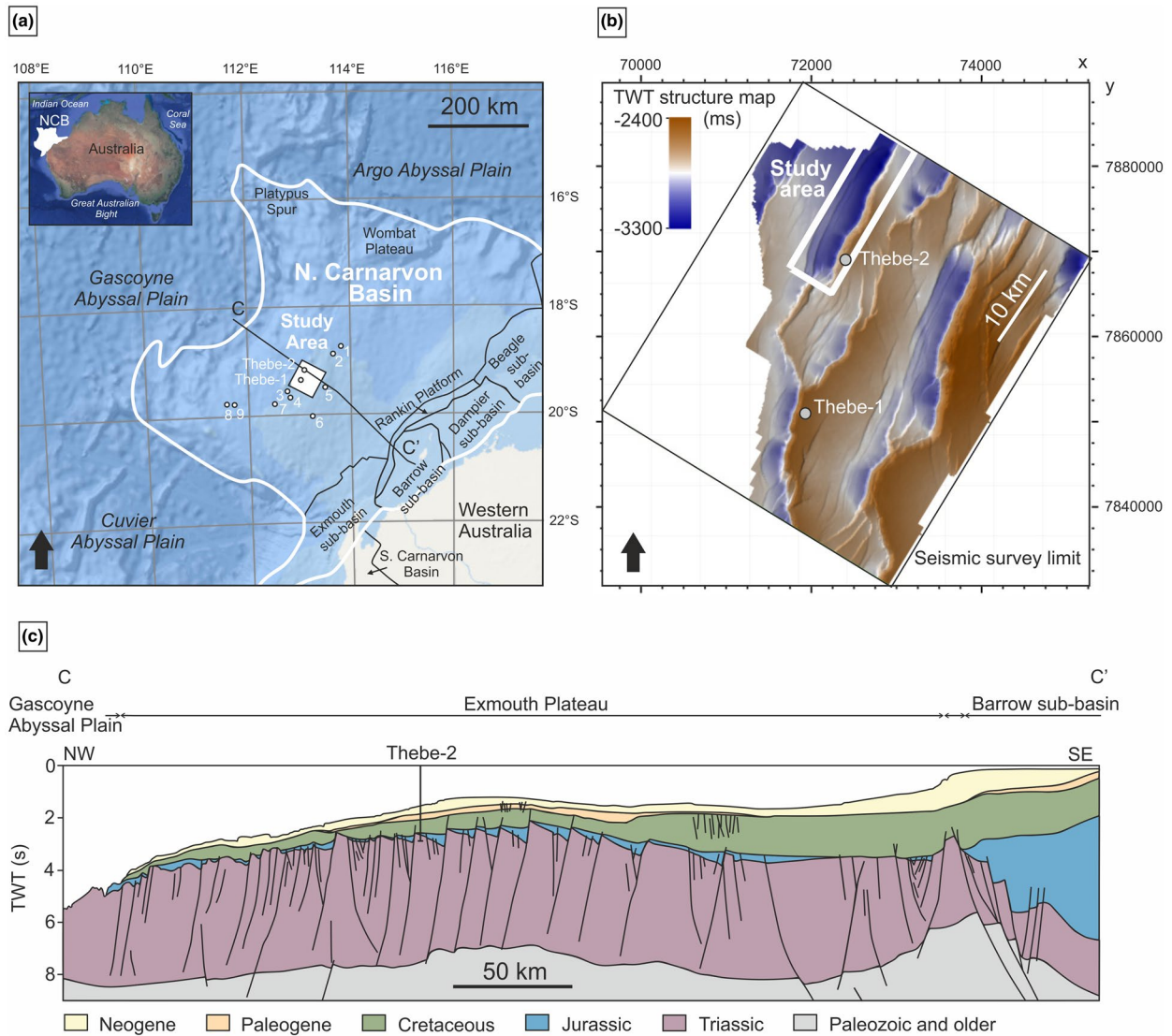


FIGURE 2 Study area location. (a) Regional map of the NW Shelf, Australia. White box indicates seismic data extent. Thebe-1 and Thebe-2 wells are highlighted. Thebe-2 penetrates the studied fault block. Numbers indicate other wells referred to in the study: 1 = Belicoso-1; 2 = Dalia South-1; 3 = Guardian-1; 4 = Kentish Knock South-1; 5 = Jupiter-1; 6 = Blake-1; 7 = Arnhem-1; 8 = Cadwallon-1; 9 = Genseric-1. (b) A time structure map (TWT) of the Top Pre-Rift surface (TR30.1 TS) is presented to highlight the faults within the seismic dataset. The specific study area covers the most north-western fault block; the Thebe-2 well penetrates the footwall of the fault. (c) Regional schematic dip-section, with the position of the Thebe-2 well (modified from Geoscience Australia). Section position shown in A (C-C')

Cretaceous Lower Barrow Group (Ellis, Woodall, Goody, Lim, & Locke, 2009a, 2009b).

3 | GEOLOGICAL CONTEXT

The break-up of Gondwanaland resulted in multiple episodes of rifting on the NW Shelf during the Paleozoic and Mesozoic (Figure 3). The Late Carboniferous to Late Permian was characterized by the break-away of the Sibamasu block, and resulted in the development of the Westralian Superbasin and the formation of the NE-trending structural grain that dominates the NW Shelf (Bradshaw et al., 1994; Deng &

McClay, 2019; Etheridge & O'Brien, 1994; L'Anson, Elders, & McHarg, 2019; Yeates et al., 1987). Following extension, a post-rift thermal sag basin developed during the Triassic, which some authors argue was punctuated by shorter periods of compression (e.g. Fitzroy Movement; Bradshaw et al., 1994; Forman & Wales, 1981; Gartrell, Keep, van der Reit, Paterniti, & Ban, 2019; Longley et al., 2002). During this time, a thick succession of marine to non-marine (Locker Shale and Mungaroo Formation) sediments were deposited (Longley et al., 2002; Marshall & Lang, 2013).

A major period of WNW-ESE-directed extension in the Late Triassic-Jurassic (Figure 3) was responsible for the disintegration of Argoland (a crustal block of the

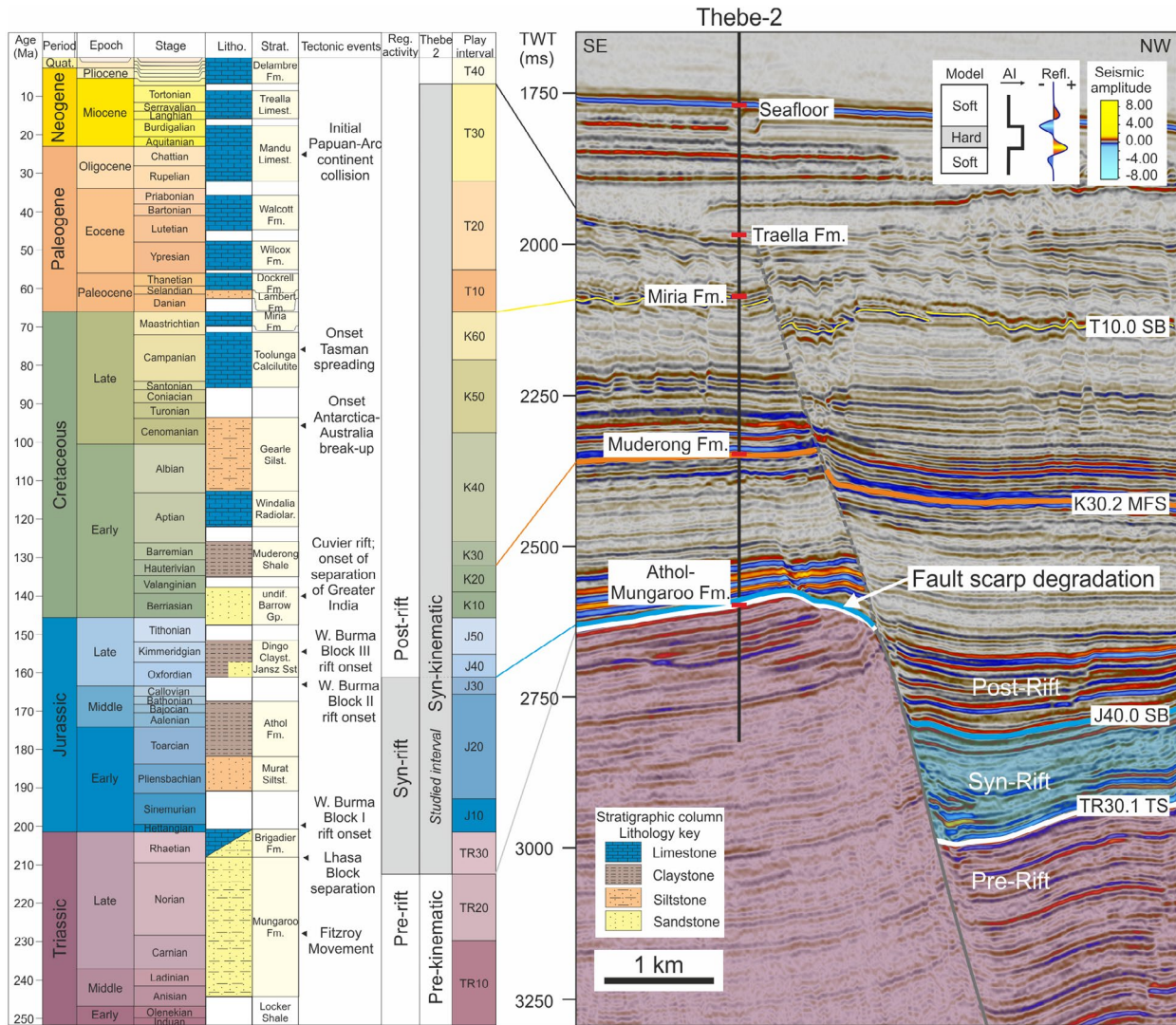


FIGURE 3 Stratigraphy of the northern Carnarvon Basin with formation tops from the Thebe-2 well presented on a NW-SE seismic section. The syn-kinematic interval of this fault is between the TR30.1 transgressive surface and J40.0 sequence boundary, which is expressed as a vertical succession in the hangingwall (blue shading), and a surface in the footwall. Inset shows seismic polarity convention and associated colour scale. Pre-rift stratigraphy is shaded in pink. TS, Transgressive surface; MFS, Maximum flooding surface; SB, sequence boundary. Tectonic events from Longley et al. (2002). Regional play intervals (stratigraphic intervals) from McArthur, Hartley, et al. (2016)

northern Gondwana margin) and the formation of the northern Carnarvon Basin sub-basins, exploiting older structural fabrics (Heine & Müller, 2005; Longley et al., 2002). The Lhasa micro-plate separated from Gondwana during the Norian (Metcalf, 1999) and the West Burma micro-plate separated over three phases spanning the Hettangian (earliest Jurassic) to Kimmeridgian (Late Jurassic; Longley et al., 2002). Deep, inboard sub-basins received abundant syn-rift sediments throughout the Jurassic, accumulating a >6 km thick succession (Deng & McClay, 2019). However, the Exmouth Plateau experienced more distributed extension, associated with the growth of relatively small-scale faults, and was sediment starved. Here, a condensed (<400 m thick) siltstone succession was deposited, represented by

the Murat and Athol formations (Bilal et al., 2018; Gartrell et al., 2016; Marshall & Lang, 2013). The Oxfordian J40.0 SB (Marshall & Lang, 2013) defines the general cessation of fault activity across the Exmouth Plateau.

After a period of tectonic quiescence, renewed rifting across the basin occurred during the Berriasian (Early Cretaceous) resulting in the separation of Greater India, deposition of the Barrow Group, and formation of the Gascoyne and Cuvier oceanic abyssal plains (Gibbons et al., 2012; Heine & Müller, 2005; Longley et al., 2002; Veevers, 1988). Valanginian-Aptian marine shales (Muderong Formation) comprise the early post-rift succession and act as regional seals to Late Triassic-Early Cretaceous hydrocarbon reservoirs (Bradshaw et al., 1988; Tindale et al., 1998). Carbonate

deposition replaced siliciclastic during the Late Cretaceous (Bradshaw et al., 1994). Post-rift regional tectonic activity first occurred during the Campanian (Late Cretaceous) in response to far-field plate motion on the southern Australian margin. This activity resulted in transpressional growth of pre-existing normal faults (Bradshaw et al., 1988; Tindale et al., 1998). Subsequently, during the Neogene, collision between the Australian plate and the Java-Banda arc (SE Asia) caused inversion and reactivation of faults across the northern Carnarvon Basin (Deng & McClay, 2019; Hengesh & Whitney, 2016; Keep, Powell, & Baillie, 1998; Figure 3).

In this study, we focus upon stratigraphy between TR30.1 TS and J40.0 SB. This is considered to be the main syn-rift episode across the Exmouth Plateau (Longley et al., 2002), but in our data, we recognize minor across-fault thickening and offsets in the higher stratigraphy, up to the Traella Fm (Figure 3). Thus, fault activity was clearly long-lasting, and our studied interval represents the early syn-kinematic stage of faulting for Thebe-2, when the greatest across-fault thickening and fault scarp degradation occurred (Figure 3).

4 | DATASET

We use a full angle PSTM (Pre-Stack Time Migrated) 3D seismic reflection dataset (HEX07B) that covers an 1800 km² area around the Thebe discovery, and well-log data from the Thebe-2 appraisal well (Ellis et al., 2009a, 2009b; Figure 2). Other nearby wells that are similarly positioned on footwall highs are used for stratigraphic comparisons; Thebe-1, Kentish Knock-1, Blake-1, Dalia South-1, Genseric-1, Guardian-1, Arnhem-1, Cadwallon-1, Jupiter-1 and Belicoso-1 (Allen, Van der Aa, Rodger, & Ellis, 2013; Ellis, 2010a, 2010b; Ellis, Woodall, Goody, Lim, & Locke, 2008; Forster, 2016; Monro, 2012; Phillips Australian Oil Company, 1980; Sturrock, 2011; Taylor, 2008, 2012). The seismic reflection data were acquired in 2007 with a Bolt airgun array (2000 psi) and 8 × 3600 m streamer cables with 100 m spacing, reaching a maximum penetration of 4609.5 ms TWT. Inlines trend NW and crosslines NE, with an interval of 25 and 12.5 m, respectively. Seismic reflection data are displayed as zero phase and with the European-Australian normal polarity convention, whereby a downwards increase in acoustic impedance corresponds to a negative reflection; i.e. ‘trough-peak-trough’ is presented with ‘red-blue-red’ colours on our seismic profiles (Figure 3). All seismic reflection sections are presented with c. 5x vertical exaggeration. Seismic frequency within the interval of interest (~2500 to 3200 ms TWT) ranges from 15 to 65 Hz, with an average of 40 Hz. At the Thebe-2 well, the seafloor is penetrated at 1,348 mTVD. All well data are presented from the rotary table depth reference point (RT), which is 22.3 m above mean sea level. Due to effects of the deep (>1000 m) water column on velocity,

average velocity data has been calculated from the seabed downwards. The average velocity at the Top Pre-Rift surface in the Thebe-2 well is 2064 m/s. Using that velocity, the average wavelength of the data in the interval of interest is ~34 m, which yields an estimated maximum vertical resolution of 8.5 m ($\lambda/4$) and a limit of detectability of 1.1 m ($\lambda/30$; Kallweit & Wood, 1982; Widess, 1973). Key formation tops (TR30.1 TS and J40.0 SB) were interpreted from well log data (Ellis et al., 2009b) and formed the basis for regional seismic mapping (Figure 3). In the seismic data, both surfaces are represented by laterally-continuous, high amplitude reflections, with TR30.1 TS and J40.0 SB characterized by soft and hard responses, respectively. Data used in this study is open-access and can be downloaded from the NOPIMS (National Offshore Petroleum Information Management System) online data repository (<https://nopims.dmp.wa.gov.au/nopims>).

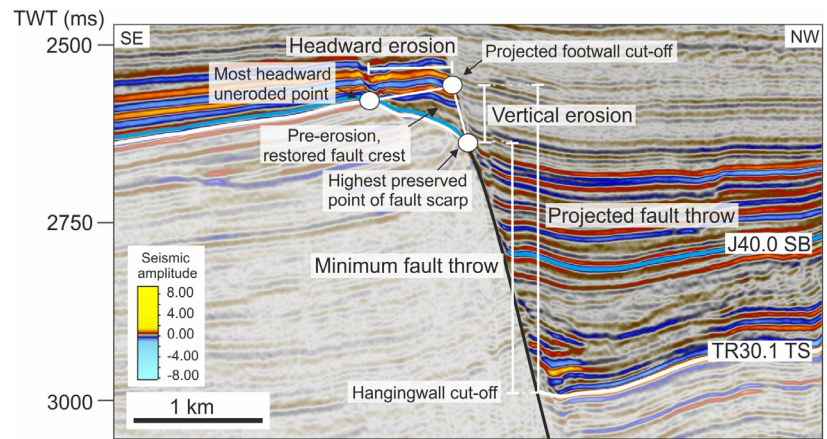
5 | METHODS

In order to understand the tectono-sedimentary evolution of the basin, and to locate the position of fixed drainage systems in the footwall that supplied the hangingwall basin, the following steps were taken.

5.1 | Footwall data analysis

Our interpretation of the depositional environment and most fundamentally, water depth, was supported by rather limited well data penetrating the immediate footwall of the Thebe-2 fault block. The Thebe-2 well is positioned towards the southern tip of the Thebe-2 fault, c. 1 km ESE of the nearest fault scarp; it does not penetrate the erosion surface defining the base of the degradation complex at the fault block crest, nor the rocks filling it (Figures 4 and 5). Between the early post-rift Kimmeridgian Marl above (~2,209.2–2211.6 mTVD) and the pre-rift Mungaroo Fm. below (~2,210.6–2213.4 mTVD), only 2–3 m of stratigraphy of indeterminate age is identified, which is inferred to represent the regional syn-rift interval (Athol and Murat formations). Cuttings indicate that the interval comprises micromicaceous and slightly calcareous claystone, containing traces of pyrite and common pelletal glauconite (Ellis et al., 2009b). A sharp decrease in gamma and increase in sonic and density readings mark the base of this thin interval. Thebe-1 is 18.6 km to the SSW of Thebe-2, also in the footwall high of an adjacent sub-basin, and similarly exhibits a 5 m interval of claystones with minor glauconite and shell fragments (Ellis et al., 2008). Taken together, these data are somewhat non-diagnostic of the depositional environment and water depth in the immediate footwall of

FIGURE 4 Positions on the fault that are used for measuring fault throw, and headward and vertical erosion, associated with fault scarp degradation. Pre-rift stratigraphy is shaded translucent white



the Thebe-2 fault block or its adjacent hangingwall. The presence of glauconite and shell fragments in the inferred syn-rift unit are at least broadly consistent with marine conditions, with claystone indicative of a relatively low-energy environment. However, uncertainty in the precise age of this unit, in addition to the chronostratigraphic and lithological characteristics of its bounding surfaces (e.g. presence of palaeosols or long-duration unconformities), mean we must use observations from the adjacent hangingwall to develop our interpretation of environment and water depth.

5.2 | Hangingwall stratigraphic analysis

Due to a lack of data to help constrain depositional environment and water depth in the footwall of the Thebe-2 fault block, we focussed on adjacent hangingwall deposits. A seismic-stratigraphic framework was established through assessment of seismic facies (SF) changes (Table 1), relative bedding dips and stratal terminations (onlap, downlap, truncation), distinguishing several key surfaces and seismic units. Interpretations of seismic facies are based upon diagnostic geometries (Table 1) and informed by the literature focused on depositional environments in modern (e.g. Cotterill, 2002; McNeill et al., 2005; Papadopoulos & Pavlides, 1992; Pechlivanidou et al., 2018; Stiros, Marangou, & Arnold, 1994), subsurface (e.g. Henstra, Gawthorpe, Helland-Hansen, Ravnås, & Rotevatn, 2017; Ravnås & Steel, 1998; Turner et al., 2018) and exposed ancient rift basins (e.g. Barrett, Collier, et al., 2019; Barrett, Gawthorpe, Collier, Hodgson, & Cullen, 2019; Cullen, Collier, Gawthorpe, Hodgson, & Barrett, 2019; Dart, Collier, Gawthorpe, Keller, & Nichols, 1994; Gawthorpe & Leeder, 2000; Leppard & Gawthorpe, 2006; Muravchik, Gawthorpe, Sharp, Rarity, & Hodgetts, 2018). Units are defined based on observations and sequence stratigraphic significance is not assumed. The top and base of each unit were mapped manually at high resolution (every inline and

crossline). Mapped surfaces change character and merge laterally. As such, some seismic units interfinger in some places, whereas further along-strike they are stacked. A number of seismic units are restricted to and derived from the main border fault (Thebe-2, from the south-east), whereas others are restricted to and derived from the north-western parts of the basin. Each seismic unit was gridded and relative volume (see Section 5.4) was estimated. Seismic units were grouped into four sets bound by three key stratal surfaces (KSS1-3) that are defined by multiple stratal terminations and which were mapped throughout the hangingwall.

The 3D seismic reflection data and stratigraphic framework permitted geometrical analysis of the hangingwall stratigraphy, such that depositional systems could be interpreted and footwall-derived fans could be distinguished from hangingwall dip-slope- and axial-derived depositional systems. 'Fans' includes fan deltas, slope aprons or submarine fans, which are identified based on their geometry, along-strike seismic facies changes distinguishing an individual fan from surrounding (interfan) strata, and onlapping stratal terminations. We specify fan deltas (SF1b; Table 1) based upon the presence of clinofolds with clearly established topsets and radial geometries in 3D. Slope apron and submarine fans exhibit planar-concave sloping reflectors (SF1a; Table 1) and are differentiated based on their basal position (Figure 1) and relative dip; i.e. slope aprons are inferred to be steeper than submarine fans. Footwall-derived fans are interpreted based on their positioning in the immediate hangingwall and reflections that dip away from the Thebe-2 fault, even after accounting for structurally-induced dip. Hangingwall- and axial-derived fans exhibit similar characteristics, but their basal positioning and overall dip direction differentiates them.

5.3 | Measurement of footwall degradation

To best assess the geometry of the degraded fault scarp, seismic mapping was undertaken of the Mungaroo Fm. surface,

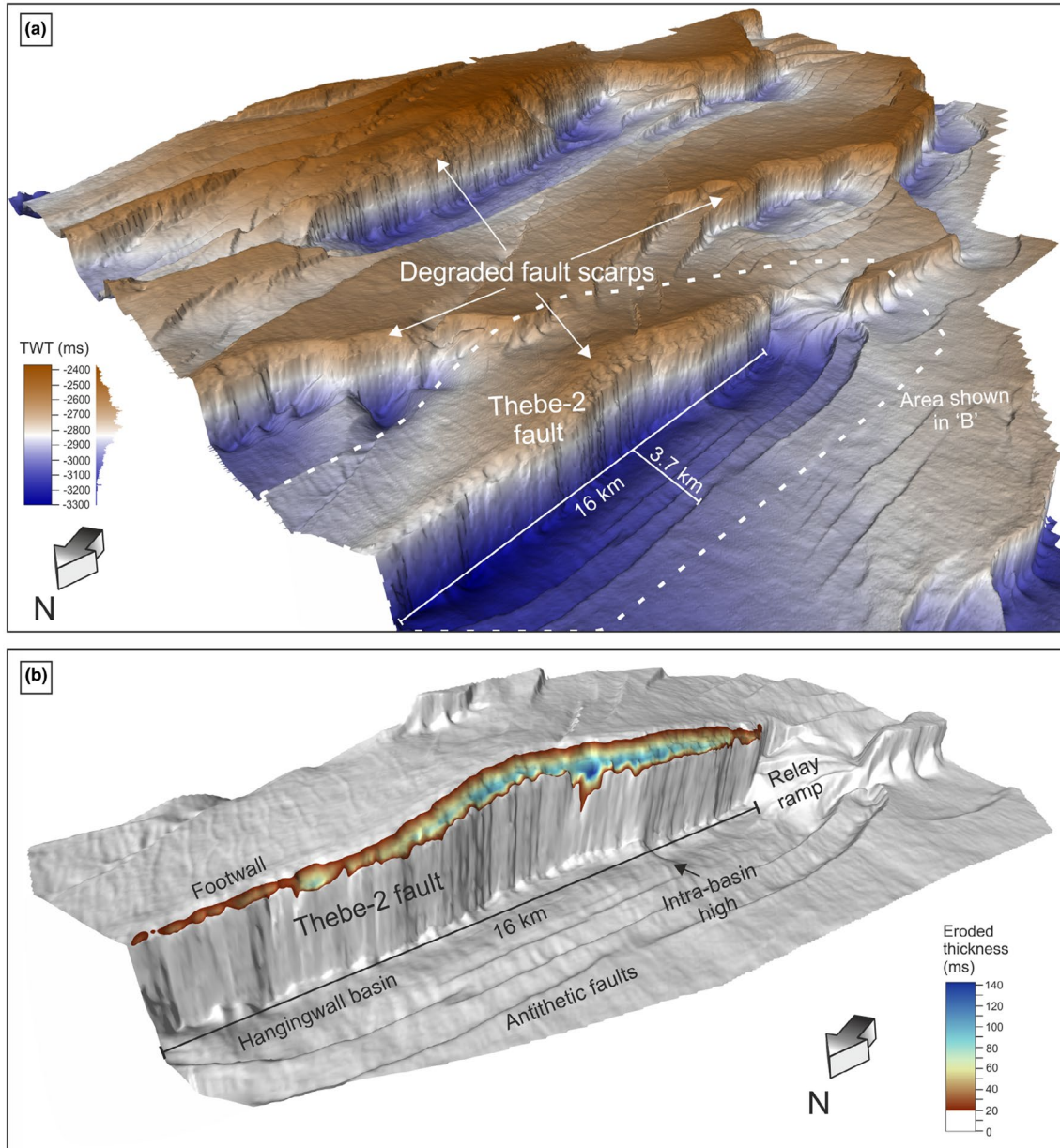


FIGURE 5 (a) 3D capture of the Top Pre-Rift surface (TR30.1 TS) across the seismic dataset to reveal a series of normal fault blocks with degraded fault scarps. (b) 3D image of the Thebe-2 fault in the study area (position shown in 'A' with white dashed outline). A map of the eroded thickness of sediment is overlain onto the degraded fault scarp. Eroded thickness colour map from Crameri (2018)

which extends across the seismic volume (Figures 4 and 5). The surface forms the interface between truncated pre-rift strata and onlapping strata. A pseudo-surface was then extrapolated by projecting the fault plane and the trend of the uneroded footwall top surface (Figure 4). This pseudo-surface was then used to estimate the footwall geometry prior to erosion. The difference in vertical height between the highest point on the restored footwall (projected footwall cut-off) to the highest preserved point on the fault scarp is taken as the amount of *vertical erosion*. The distance between the highest point on the restored footwall to the most headward uneroded point on the footwall top surface

is taken as the amount of *headward erosion* (Figure 4). Uncertainty in these measurements, which propagates into the associated volume calculation (see below), relates to the accuracy with which we are able to assess the pre-erosion footwall geometry. This in turn is related to how accurately we extrapolate the fault plane and uneroded footwall top surface (Figure 4). The volume between the restored footwall pseudo-surface and the Top Pre-Rift surface represents the total amount of erosion of the footwall along the fault block crest (shown in cross-section in Figure 4). We estimated 'projected' fault throw every 5 inlines (125 m) by manually measuring the distance between the *projected*

TABLE 1 Seismic facies (SF): example extracts, descriptions, interpretations and analogues

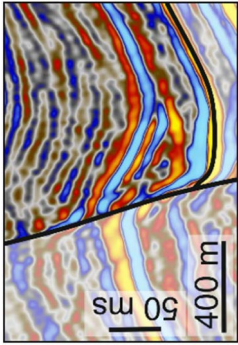
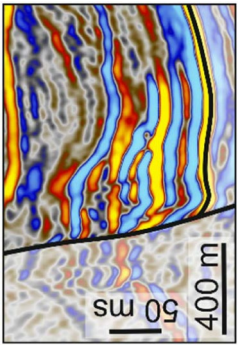
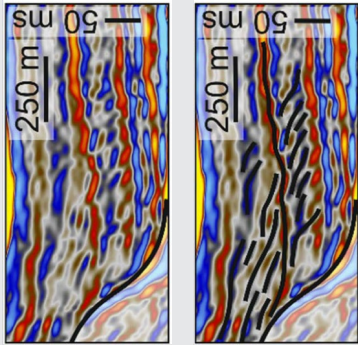
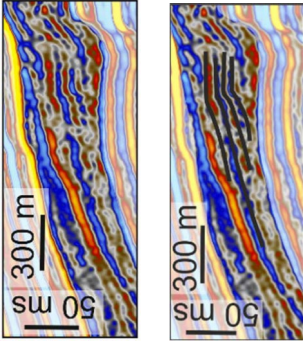
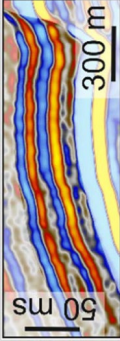
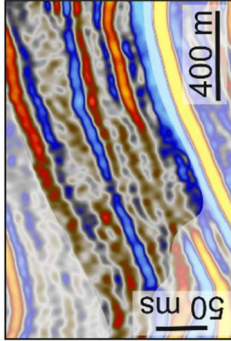
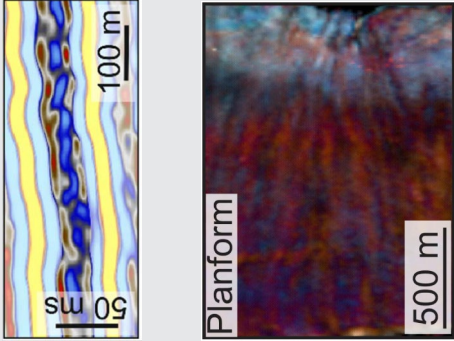
Seismic facies	Example	Description	Interpretation	Analogues
SF1	<p>a) </p> <p>b) </p>	<p><i>Character:</i> Mainly high amplitude, low-med. frequency (10–50 Hz), steeply-dipping reflections, even after correcting for the structurally-induced dips. Internal reflections range from continuous to chaotic.</p> <p><i>Geometry:</i></p> <p>a) Planar-slightly concaved slope. 3D prism-apron shape along the fault. No radial geometry.</p> <p>b) Flat-slope clinoform. 3D radial geometry and in some cases interfingering with adjacent fans. Foreset heights ranges from 40–200 ms (70–350 m with 1742 m/s velocity).</p> <p>Internal architectures vary along-strike, but generally exhibit progradational stacking near the base, and aggradational or retrogradational stacking towards the tops of the fans.</p> <p><i>Position:</i> Always positioned in the immediate hangingwall and dipping away from the main border fault.</p> <p>a. Sloping reflections continue along the fault <4 km and extend <650 m away from the fault.</p> <p>b. Numerous positions – most striking example is ~4.5 km from the southern end of the basin</p>	<p>Footwall-derived fans:</p> <p>a) Slope apron</p> <p>b) Fan delta</p>	<p>SF1a: Xylokaastro horst, Gulf of Corinth (Cullen et al., 2019)</p> <p>Lower Rudeis Formation, Hammam, Suez Rift (Leppard & Gawthorpe, 2006).</p> <p>SF1b: Pleistocene (exposed) and Pliocene (submerged) fan deltas, Gulf of Corinth (Barrett, Gawthorpe, et al., 2019; Barrett, et al., 2019; Ford et al., 2007; Gobbo et al., 2015).</p> <p>Brae play, ‘T’ and ‘Tree’ fields, North Sea (Turner et al., 2018 and references therein)</p>
SF2		<p><i>Character:</i> Low-med. amplitude (peaks brighter than troughs), low-med. frequency (10–50 Hz), discontinuous, dipping reflections. Separated by high amplitude, flat-lying reflections that are conformable.</p> <p><i>Geometry:</i> 3D radial geometry. Foreset height 20–40 ms (35–70 m with 1742 m/s velocity). Foresets exhibit a highly progradational stacking pattern.</p> <p><i>Position:</i> Foresets prograde from the northern fault tip in a direction parallel to the fault trend, i.e. the depositional system follows an axial route. Foresets are restricted to a single interval/unit and are confined laterally and at their distal extent by footwall-derived fans.</p> <p>Only occurs in Unit G.</p>	<p>Stacked, prograding fan delta foresets, separated by flooding surfaces.</p>	<p>Evrostini and Selinous fan deltas, Gulf of Corinth (Barrett, Gawthorpe, et al., 2019; Rohais, Eschard, & Guillocheau, 2008)</p>

TABLE 1 (Continued)

Seismic facies	Example	Description	Interpretation	Analogues
SF3		<p><i>Character:</i> Medium amplitude, med. to high frequency (40–70 Hz) reflections with moderate continuity.</p> <p><i>Geometry:</i> Low-angle, basinward-dipping with clinoformal and radial shape. Foreset height 50–60 ms (90–105 m with 1742 m/s). Topset length <300 m.</p> <p><i>Position:</i> Prograding away from antithetic faults into the southern sub-basin. Occurs only in Unit G.</p>	Deltaic clinoforms prograding basinward from antithetic faults	Kremida Fm., Megara Basin (Bentham, Collier, Gawthorpe, Leeder, & Stark, 1991). Rudeis Fm., Suez Rift (Muravchik et al., 2018).
SF4		Medium to high amplitude, low-high frequency (20–70 Hz), moderate-high continuity, undulating reflections that are relatively flat-lying to gently-dipping (sometimes following pre-rift topography) and fade/pinch-out down-dip and along-strike, or onlap/downlap underlying topography. Observed in Units A, B, F, I, J, K, L.	Turbidites and pelagic/hemipelagic fall-out.	Early Palaeogene, Santos Basin, Brazil (Stevenson, Jackson, Hodgson, & Johnson, 2019). The Magdalena Fan, offshore Colombia (Ortiz-Karpf, Hodgson, & McCaffrey, 2015).
SF5		Low amplitude, low frequency (10–20 Hz), chaotic-discontinuous reflections. Apparent at the downdip terminations of higher amplitude, dipping reflections. Observed in Units B, C, D, E, F, G, H, I, K.	Mass transport deposits/hemipelagic fall-out in clinoform bottomsets	Early Palaeogene, Santos Basin, Brazil (Stevenson et al., 2019). The Magdalena Fan, offshore Colombia (Ortiz-Karpf et al., 2015).
SF6		Med. amplitude, low-high frequency (10–80 Hz), discontinuous reflections with undulating geometries. Observed in the lowest syn-rift stratigraphy (Unit A). In planform, straight-sinuuous approx. E-W trending features are apparent, using spectral decomposition (R, G, B = 21, 32, 39 Hz). The lineaments appear to be distributive in nature.	Fluvial channels?	Mungaroo Fm. NW Shelf, Australia Heldreich et al. (2017)

footwall cut-off point and the *observed hangingwall cut-off* (Figure 4). 'Minimum' fault throw is provided by measuring the distance between the highest preserved point on the fault scarp to the hangingwall cut-off; omitting the eroded part of the fault scarp in the measurement (Figure 4).

5.4 | Volume calculations

A volume balancing approach was developed to compare the amount of sediment in the hangingwall (V_{HW}) to the amount of material eroded from the adjacent footwall (V_{FW}). For the latter, a 3D grid was constructed between the extrapolated pseudo-surface (restored footwall crest) and the Top Pre-Rift surface (Figures 5b and 6). From this, the eroded thickness (1D) and eroded bulk volume (3D) of sediment was calculated.

To calculate the volume of sediment in the hangingwall, the two seismic units comprising radial, basinward-dipping reflections (Units E and H), were interpreted to represent footwall-derived fans (SF1a and SF1b, Table 1; Section 6). The base and top of these units were mapped, the areas between them were gridded, and the bulk volumes were calculated using the same approach as defined above for the footwall (Figure 7).

Because the seismic reflection data are presented in time, the output volumes are not true volumes of eroded and deposited sediment. To augment comparisons along-strike, and to avoid physically unrealistic units, a ratio is presented of hangingwall-fill to footwall erosion (V_{HW}/V_{FW} ; Figure 7). Each millisecond (TWT) on the vertical axis of a grid cell is assumed to represent one metre in the volume calculation (a velocity of 2000 m/s; Figure 8). The Top Pre-Rift surface in the Thebe-2 well (in the footwall) lies at 2,632 ms (TWT) in the seismic data, where checkshot data yield an average velocity of 2066 m/s (Figure 8a). This was averaged from the first checkshot below the seabed (1,430 m MD; 1,870 ms TWT seismic) to the Top Pre-Rift surface (2,217 m MD; 1,750 ms TWT seismic; Figure 8a). One millisecond (TWT) at that depth represents 1.03 m (Figure 8a,b). The interval velocity at the position of the Top Pre-Rift surface is 2,182 m/s and so each millisecond (TWT) in that interval could represent up to 1.09 m (TWT; Figure 8b). Therefore, the range of estimates for the vertical axis of a footwall grid cell based on average and interval velocities is therefore 1.03–1.09 m (Figure 8b). This is up to 10% larger than the 1 m assumption for the vertical axis of a grid cell used in the volume calculation for both the footwall and hangingwall, and so all 'volumes' represent minimum values and could be underestimated by <10%.

Another assumption is that a grid cell volume in the footwall is equivalent to one in the hangingwall, which is uncertain due to the lack of depth conversion and no wells penetrating the hangingwall. We can reduce some uncertainty

by extrapolating velocity data in the footwall to the depth of the tops of the hangingwall fans to account for the expected increase in velocity with depth (Figure 8b). The *average* velocity trend from the seabed to the Top-Pre-Rift surface is extrapolated to 3000 ms TWT (yellow lines in Figure 8b). The pre-rift succession, including the gas-bearing zone below the footwall crest, are thus omitted from the velocity trend. This gives an average velocity of 2,282 m/s at 3000 ms (TWT). One millisecond (TWT) at this depth represents 1.14 m. Following the same approach with *interval* velocity data gives 2,363 m/s at the depth equivalent to the top of the hangingwall fans (Figure 8b). In this case, one millisecond (TWT) at this depth represents up to 1.18 m. The vertical axis of a hangingwall grid cell is between 1.14–1.18 m (Figure 8b), and is therefore up to 15% thicker than a footwall cell, and thus may represent a larger volume of rock. Therefore, our approach likely underestimates hangingwall cell volume compared to footwall cell volume, which means any derived ratio (V_{HW}/V_{FW}) is a minimum estimate. The hangingwall succession is also lithologically different to that in the footwall (pre-rift succession) and likely has different acoustic properties (e.g. higher or lower density, and faster or slower acoustic velocity).

Our volume balancing approach would be more effective with depth-converted data. However, no hangingwall basins are drilled across the Exmouth Plateau, meaning any velocity model-based depth conversion would be uncertain. Nonetheless, our approach could be applied to depth-converted data elsewhere, or TWT data if the appropriate uncertainties outlined above are considered.

5.5 | V_{HW}/V_{FW} quadrant analysis

In order to identify where the greatest difference in hangingwall-fill to footwall erosion occurs, we assess ten paired quadrants. Quadrant boundaries are defined by lows (i.e., thin areas) in isopach maps and sharp seismic facies changes in cross-section, which broadly correspond to interfan areas (Barrett, Gawthorpe, et al., 2019) between along-strike fans in Unit E (Figure 7a). The volume of footwall erosion (V_{FW}), and volume of sediment in the hangingwall fans (V_{HW}), are calculated for each quadrant, with the exception of Quadrant 10; this is omitted from our analysis due to significant uncertainty in the erosion measurements in the proximity of the relay zone. Only seismic units that are confidently interpreted to be characterized by footwall-derived hangingwall fans are included in the analysis. Other hangingwall sources are therefore not considered to contribute to the volumes calculated. There are three main assumptions and considerations in our quadrant analysis: (a) all footwall-derived material is encompassed within each hangingwall quadrant, although some finer-grained, buoyant material may have bypassed

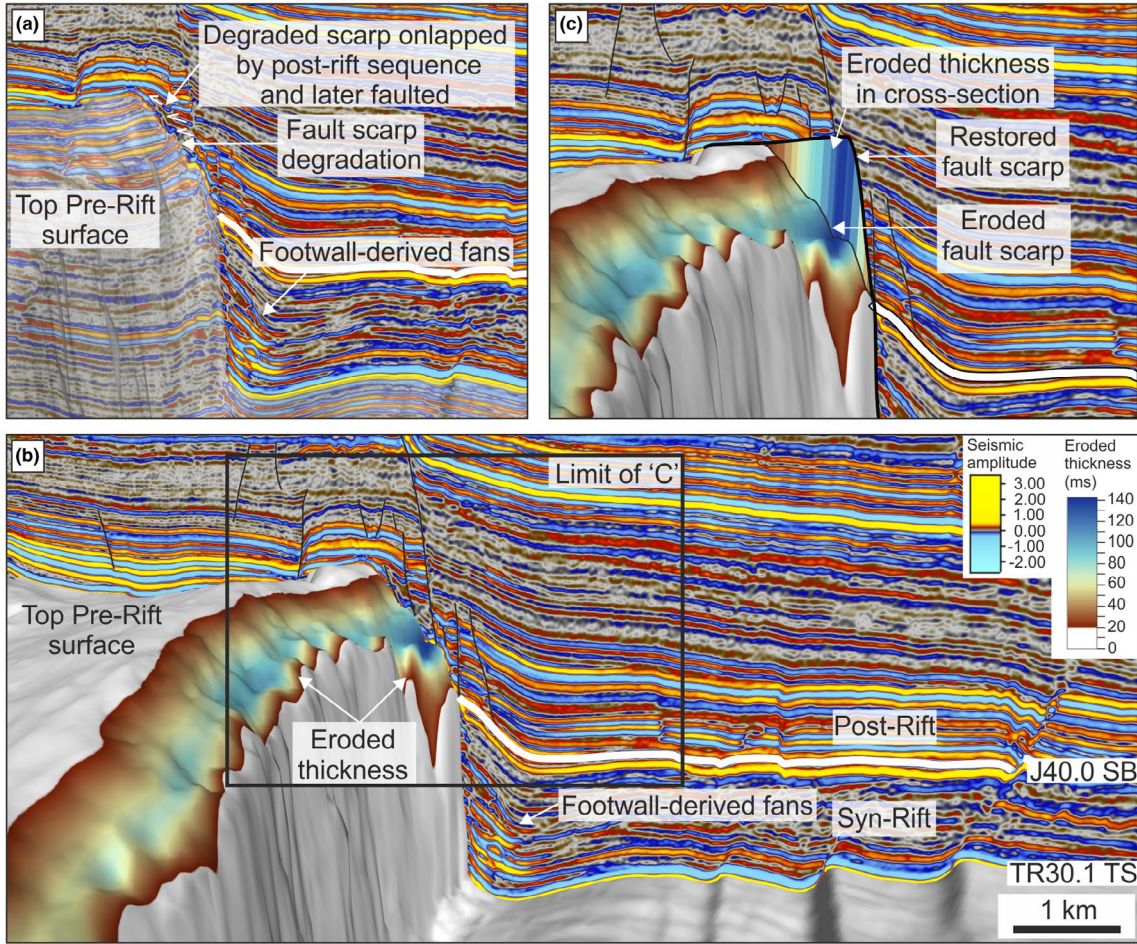


FIGURE 6 Seismic cross-section to highlight the degraded fault scarp. (a) Degraded area of the fault scarp is onlapped and filled by strata post-dating J40.0 SB. Transparency is applied to the Top Pre-Rift surface (TR30.1 TS) to reveal the footwall seismic character. (b) Map of the eroded thickness of sediment is overlain onto the fault scarp. (c) Zoomed in area of 'B' to show eroded thickness of the footwall projected onto the seismic cross-section. SB, sequence boundary. Eroded thickness colour map from Cramer (2018)

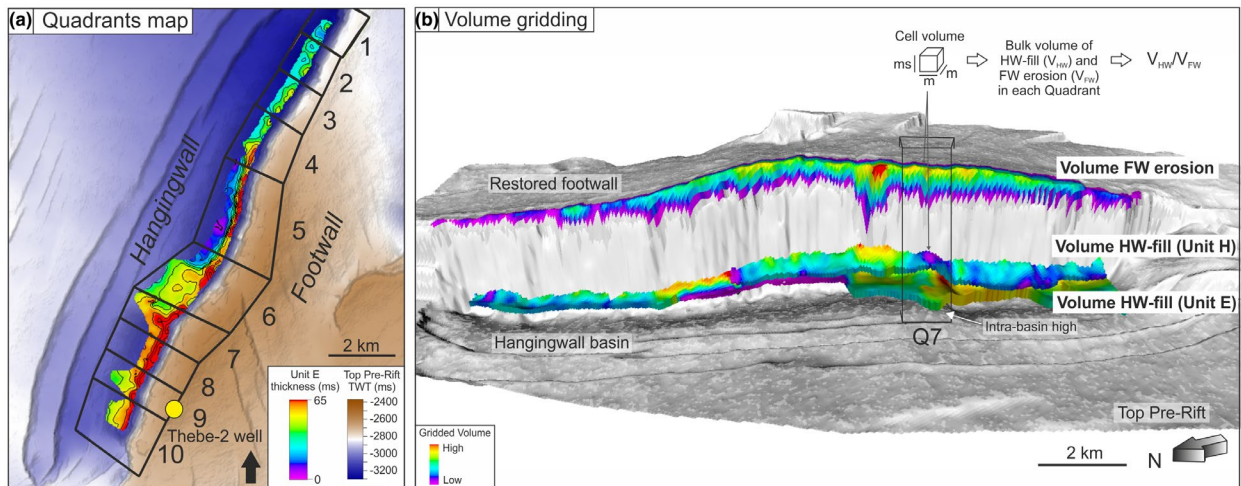


FIGURE 7 Methodology for volume balancing approach (V_{HW}/V_{FW}). (a) Layout of quadrants along the fault for analysis. Quadrant boundaries are defined by interfan areas in the hangingwall basin, demonstrated here with an isochron map of Unit E, containing footwall-derived fans. Each quadrant encompasses an area of the footwall and hangingwall. (b) Volume gridding approach of the hangingwall units (Units E and H) containing footwall-derived fans, and eroded material from the footwall. The restored footwall to its pre-erosional state is presented. HW, hangingwall; FW, footwall

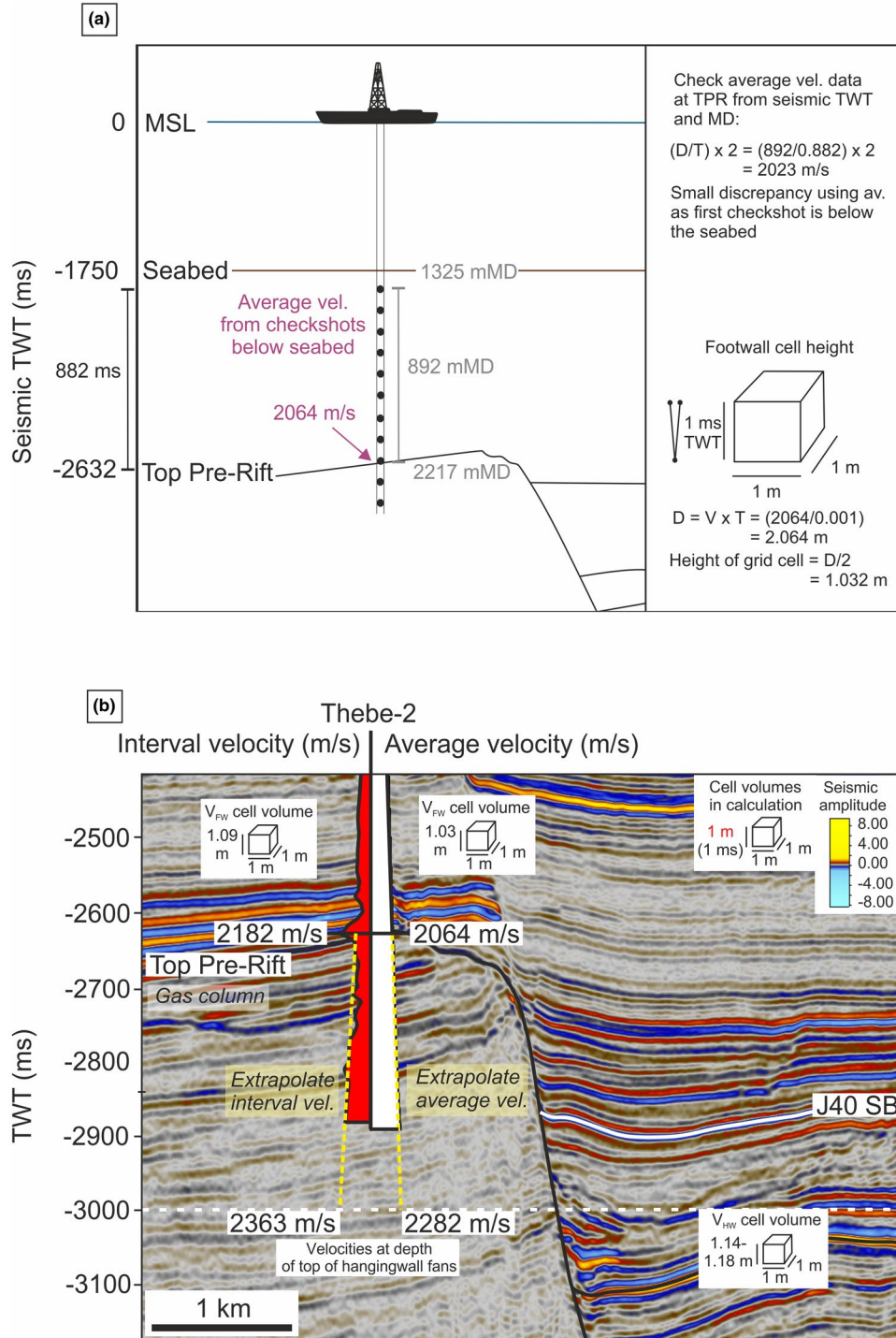


FIGURE 8 Approach for validating cell volume equivalency between the footwall (where there is velocity data from the Thebe-2 well) and the hangingwall (where there is no velocity data). 1 ms (TWT) is assumed to represent 1 m vertical height of a cell for both footwall and hangingwall intervals in volume calculations; here we check if that assumption is valid. (a) Approach for calculating grid cell height in the footwall using the average velocity trend from checkshot data (1.03 m). Average is taken from the first checkshot to the Top-Pre-Rift surface and is verified using seismic TWT data and the measured depth (MD) in the well. TWT, two-way time; TPR, Top Pre-Rift surface; D, distance; V, velocity; T, time. (b) Approach for calculating grid cell height in the hangingwall. Velocities are extrapolated from the seabed to the Top Pre-Rift surface, thus excluding the pre-rift succession and gas-bearing sediments from the trend. This gives vertical cell heights of 1.14–1.18 m for the hangingwall fans. Various assumptions are inclusive of this approach (see text). Hangingwall cell volumes are thus shown to be underestimated by up to 15% relative to footwall cell volumes, hence volume balance estimates represent minimum values

the mapped area of the fans, may have been re-distributed along-strike or may have exited the basin; (b) the degraded footwall area within each quadrant supplies the hangingwall area within the same quadrant; i.e. there is no oblique supply between quadrants; (c) all eroded material from the footwall is preserved in Units E and H. Footwall-derived components are identified in other hangingwall units that could have come from fault scarp degradation (Section 6.1). If considered in the analysis, they would increase hangingwall relative to footwall volumes and thus would support any hangingwall excess. All assumptions yield minimum estimates for hangingwall volume in each quadrant.

The difference between V_{HW} and V_{FW} , and the V_{HW}/V_{FW} ratio are recorded for each quadrant. Any excess volume in the footwall-derived hangingwall fans (i.e. $V_{HW} > V_{FW}$ or $V_{HW}/V_{FW} > 1$) is interpreted to be a result of through-going sediment transport from beyond the footwall crest. Any excess eroded volume in the footwall (i.e. $V_{FW} > V_{HW}$ or $V_{HW}/V_{FW} < 1$) is interpreted to be a result of sediment bypass or redistribution. Quadrants are not equal in area, but through the use of a ratio, the volumes are normalized and comparisons between quadrants can be made. Volumes are not normalized in the $V_{HW} - V_{FW}$ approach and highlight 'absolute' values of footwall erosion or hangingwall-fill excess.

6 | RESULTS

6.1 | Stratigraphic framework

For the stratigraphic framework, 12 stratal units (Units A-L) are identified in the hangingwall basin between TR30.1 TS and J40.0 SB, based on seismic facies (Table 1) and geometry (Table 2; Figures 9 and 10). The 12 stratal units are compiled into four sets (unit set 1–4), separated by key stratal surfaces (KSS1–3) and representing four stages of evolution of the basin (Figure 9b). We identified four SE-dipping antithetic faults (AA, AB, AC and AD) that strike NNE-SSW, parallel to the Thebe-2 fault and bound the basin to the west. These faults were active at various times during rifting, based on thickness patterns in adjacent syn-kinematic units. For ease of description, the hangingwall basin is divided into three sub-basins (northern, central and southern; Figure 9a). The southern and central sub-basins are separated by a topographic high that trends NW-SE. This appears to limit the extents of some units to either sub-basin (e.g., Units D and F are absent in the southern sub-basin). The central and northern sub-basins encompass the strike extents of antithetic faults AA and AB, respectively. Foreset heights are provided with depth-converted estimates using a velocity of 2320 m/s, which sits in the range provided from average and interval velocity data in the footwall (2282–2363 m/s; Section 5.4; Figure 8).

6.1.1 | Unit set 1

Unit Set 1 comprises Unit A, which is bounded by the Top Pre-Rift surface at its base and KSS1 at its top (Figures 9 and 10). KSS1 is high-amplitude and laterally-continuous in the northern sub-basin, but becomes lower amplitude and more discontinuous southward. Unit A extends across the entire hangingwall basin and is intersected by antithetic faults AA-AD. The unit has a maximum stratigraphic thickness of 63 ms (73 m) and thins southwards to ~40 ms (46 m). Overall, Unit A thickens towards the Thebe-2 fault; at the fault centre and towards the northern fault tip, this occurs in association with NW-dipping reflections that dip away from the fault (SF1b, Table 1; Figure 9b–e). Some reflections exhibit a clinoformal geometry and appear to be fan-shaped in 3D (SF1b, Table 1; Figure 9b and d); we interpret these bodies as fan deltas. Elsewhere, the unit is dominated by discontinuous, undulating reflectors in cross-section, with E-W trending, curvilinear planform expressions apparent through spectral decomposition, which could represent distributary channels, similar to those in the underlying Mungaroo Fm (SF6, Table 1; Figure 10).







6.1.2 | Unit set 2

Unit Set 2 comprises Units B-E, and is bounded at the base by KSS1 and at the top by KSS2 (Figures 9 and 10). KSS2 comprises two high-amplitude, laterally continuous reflections that merge down-dip. Both reflections dip towards the basin at the same stratigraphic level, one from the NW and one from the SE. KSS2 is denoted by a change of seismic facies across it and multiple downlaps from reflections above (Figures 9 and 10).

Unit B thickens into the Thebe-2 fault and slightly into the antithetic faults, AB and AC (Figure 9c,d,f), which are separated by a short relay zone (Figure 9a). Unit B exhibits slope apron deposits (SF1a, Table 1) and turbidites (SF4, Table 1). Fan-shaped, dipping reflections (SF1a, Table 1) stack against the footwall of the Thebe-2 fault, which are ~30 ms (~35 m) high and represented by single, low frequency, high amplitude wavelets (Figure 9b–d). The internal architecture of the fans is below seismic resolution. SF4 (interpreted as turbidites) is the dominant seismic facies of the depositional systems inferred to come from the west, and in this case, reflections dip gently south-eastwards (Figure 9).







Unit C is restricted to the basin centre and comprises east- and west-dipping reflections that onlap and fill the underlying topography (Unit B; Figures 9c,d and 10). Unit C is bowl-shaped and is thickest (53 ms) at its centre. It is dominantly composed of low amplitude, low frequency, discontinuous reflections interpreted to be a combination of mass transport deposits in clinoform bottomsets and pelagic/

TABLE 2 Stratigraphic framework: seismic unit descriptions

Unit set	Unit	Colour	Key features	Seismic facies	Extent	Fault thickening	Top surface character	Max. strat. thick.	Max. foreset height
A	1		Some small clinoforms from main border fault. Undulating, flat-lying reflectors elsewhere	SF1b; SF6	Whole basin	Main border fault	KSS1. Bright and continuous reflection in N - becomes discontinuous towards S. Change of seismic facies across surface.	63 ms	20 ms (23 m)
B	2		Some small fans from main border fault and antithetic faults	SF1a-b; SF4	Whole basin	Main border fault & AB & AC	Change of seismic facies & downlap from reflections above.	40 ms. (av. 23 ms)	30 ms (35 m)
C	2		Bowl-shaped unit. East- and west-dipping, inter-fingering reflections	SF5	Central sub-basin	None	Distinct, flat-lying, high amplitude trough, downlapped by Units E and D.	53 ms	
D	2		Depositional system from NW (antithetic faults)	SF4; SF5	Northern and central sub-basins. Restricted to the NW.	AB & AC	KSS2. In the N, downlapped by system from NW (Unit F), and towards S it is downlapped by Unit H. Change in seismic facies. In places eroded by Unit G.	80 ms (av. 43 ms)	
E	2		Large fans from main border fault.	SF1a-b	Whole basin	Main border fault	KSS2. In the N, downlapped by system from NW (Unit F), and towards S it is downlapped by Unit H. Change in seismic facies. In places eroded by Unit G.	93 ms	67 ms (78 m)
F	3		Depos. systems from the NW (antithetic faults)	SF8; SF4; SF5	North. and central sub-basins. Restrict-ed to the NW.	AA, AB, AC & AD	Downlapped by Unit G from the NW. Change in seismic facies.	80 ms	

(Continues)

TABLE 2 (Continued)

Unit set	Unit	Colour	Key features	Seismic facies	Extent	Fault thickening	Top surface character	Max. strat. thick.	Max. foreset height
G	3		Axial clinoforms between flat-lying reflections & fans from NW (antithetic faults)	SF2; SF3; SF4	Whole basin	AA, AB, AC & AD	KSS3. Onlapped by Units I, J, K, in places onto a high-amplitude approximately flat-lying trough. Change in seismic facies.	86 ms; (av. 41 ms)	Axial: 20 ms (23 m) HW-derived: 40–60 ms (46–70 m)
H	3		Large fans from main border fault	SF1a-b	Central and south sub-basins. Restricted to SE.	Main border fault	KSS3. Onlapped by Units I, J, K, in places onto a high-amplitude approximately flat-lying trough. Change in seismic facies.	98 ms	98 ms (114 m)
I	4		Passive infilling of topography	SF3; SF7	North. and central sub-basins	Main border fault	In the N sub-basin – J40 SB (high amplitude, continuous reflection). In central sub-basin – downlapped by Unit J. Change in seismic facies.	96 ms (av. 29 ms)	34 ms
J	4		Fan from main border fault + passive infilling of the basin	SF1a; SF8	Central sub-basin	Main border fault	In the central sub-basin – J40 SB (high amplitude, continuous reflection). At the basinal high, downlapped by Unit K. Change in seismic facies.	100 ms	100 ms (116 m)
K	4		Passive infilling of the basin	SF3; SF5	Central and southern sub-basins	Main border fault	Relatively flat lying, possibly erosive, high amplitude trough. Change in seismic facies.	79 ms	
L	4		Passive infilling of the basin	SF4; SF7	Southern sub-basin	Main border fault	J40 SB (high amplitude, continuous reflection).	80 ms	

Abbreviation: U, Unit.

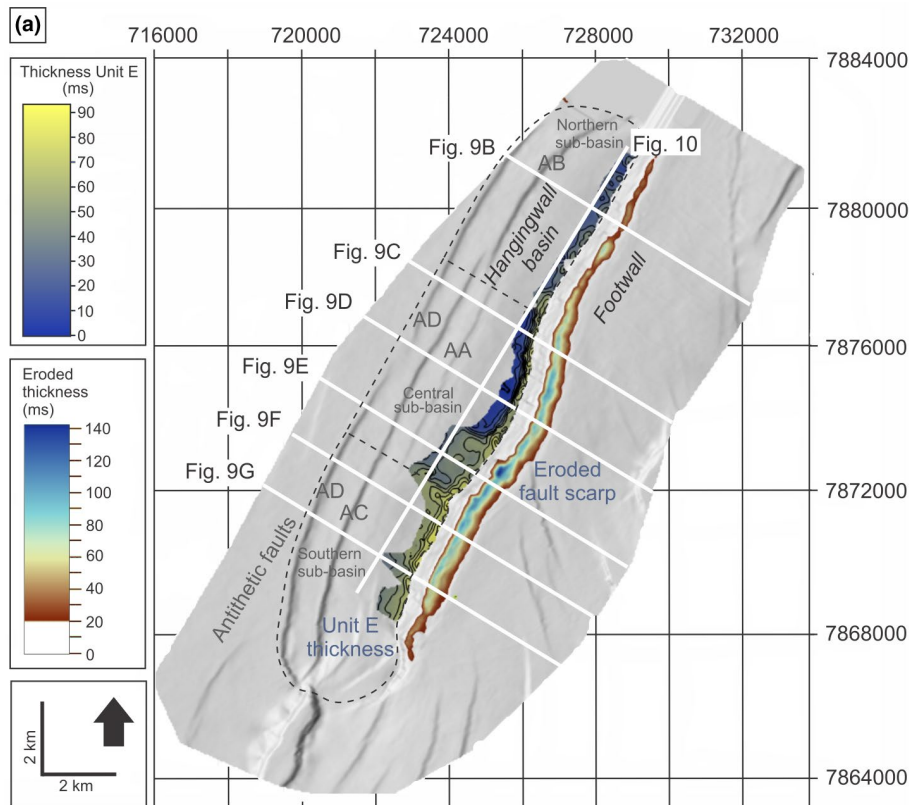


FIGURE 9 Six SE-NW trending (dip-oriented) representative seismic sections along the fault are presented to show the stratigraphic framework. (a) Map of the basin (Top Pre-Rift surface; TR30.1 TS) to show positions of seismic sections (b–g). A map of the eroded thickness of the fault scarp is overlain onto the footwall and an isochron map of Unit E is presented in the hangingwall. The basin is divided into three sub-basins for reference; northern, central and southern. Antithetic faults AA–AD are highlighted. (b–g) seismic sections with observations (upper) and interpretations (lower). Pre-rift stratigraphy is shaded white. Seismic units A–L are shaded in blues. Footwall degradation is shaded in black on interpreted sections. Key stratal surfaces (KSS) are highlighted in white. Eroded thickness colour map from Crameri (2018). Uninterpreted sections are available in the Appendix

hemipelagic fall-out (SF5, Table 1). The top of Unit C is a distinct, flat-lying, high-amplitude trough event that is downlapped by reflections within Units D and E (Figure 9c).

Unit D extends across the northern and central sub-basins (Figures 9a–e and 10), but is absent in the immediate hangingwall of the Thebe-2 fault and in the southern sub-basin (Figure 9a,f,g). The unit thickens into antithetic faults AB and AC (Figure 9b–e) and it comprises mass transport deposits and pelagic/hemipelagic fall-out (SF4 and SF5, Table 1), which dip gently towards the basin, from the NW.

Unit E is dominated by fan-shaped, dipping, clinoform-like reflection geometries (fan deltas, SF1b, Table 1; e.g. Figure 9d and g) and intervening planar-sloping geometries (slope apron deposits, SF1a, Table 1; e.g. Figure 9b,c,e) that dip away from the Thebe-2 fault and appear to be footwall-derived (Figure 9b–g). The unit extends along the entire hangingwall basin (Figure 9a), is thickest in the immediate hangingwall of the Thebe-2 fault (~93 ms) and thins towards the basin, pinching out 400–700 m from the fault. Foresets have a maximum height of 67 ms (78 m). In the north and central sub-basins,

Unit E interfingers with Unit D (e.g. Figure 9b–d), but towards the southern sub-basin, where present, it is downlapped by Unit D (Figures 9e and 10). Unit E is used for volume balancing with footwall degradation because it is one of two units (Units E and H) that are dominated by large-volume, footwall-derived fans.

6.1.3 | Unit set 3

Unit Set 3 comprises Units F–H, and is bound by KSS2 at the base and KSS3 at the top (Figures 9 and 10). KSS3 is characterized by multiple onlaps and downlaps from reflections within Unit Set 4 above. Unit F extends across the northern and central sub-basins from the west, but does not reach the Thebe-2 fault. The unit thickens into antithetic faults AB, AC and AD (Figure 9b–d), and it is dominated by possible deep-water deposits (SF4 and 5; Table 1).

Unit G extends across most of the hangingwall basin, but is absent <700 m from the Thebe-2 fault where it downlaps underlying, fan delta-related topography (Unit

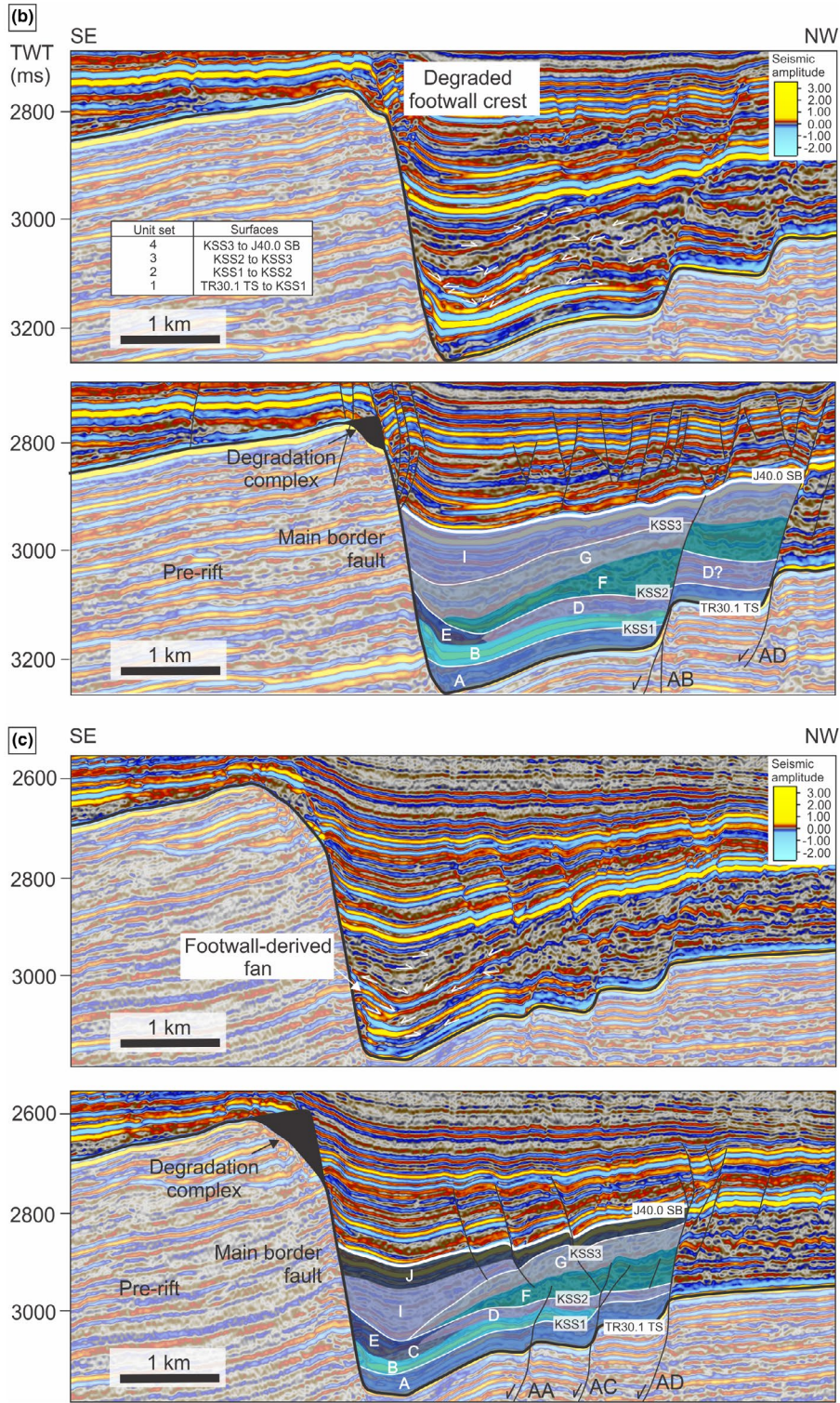


FIGURE 9 Continued

E; e.g. Figure 9f). The unit has a distinct character in the northern sub-basin, comprising two clinoform-bearing packages separated by a relatively flat-lying, low-medium amplitude reflection (SF2; Table 1; Figure 11a,e,f). Foresets within these units are ~20 ms tall (23 m), with the clinoforms prograding southwards from the northern

fault tip (Figures 10 and 11e). In the central sub-basin, the thickness of the clinoform packages decreases. South of the basal high separating the central and southern sub-basins, another set of clinoforms (SF3; ~40–60 ms; 46–70 m high) prograde south-eastwards from antithetic fault AC (Table 1; Figures 9 and 11b). The clinoforms downlap and

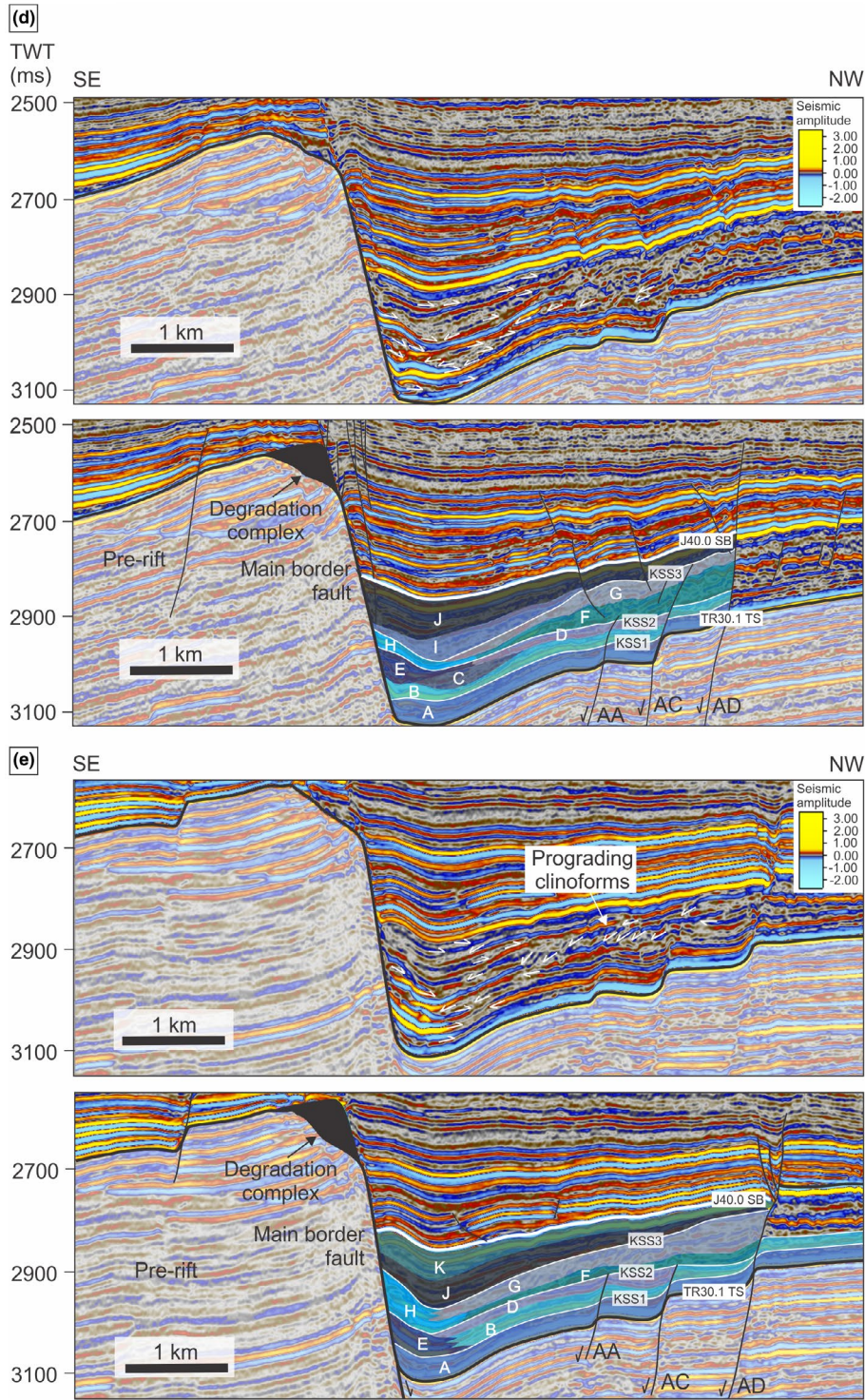


FIGURE 9 Continued

interfinge with the distal margin of fans within Unit H, with foresets decreasing in height down-dip (Figures 9d,e and 11b).

Unit H extends along the immediate hangingwall of the Thebe-2 fault in the central and southern sub-basins (Figure 9a,d-g). Similar to Unit E, Unit H comprises large

(foreset heights up to 98 ms; 114 m), footwall-derived fans (SF1a-b, Table 1) that generally dip north-westward, and pinch-out ~850 m away from the fault (Figure 9e,f). Unit H is used for volume balancing with footwall degradation because, like Unit E, it contains a substantial volume of footwall-derived deposits.

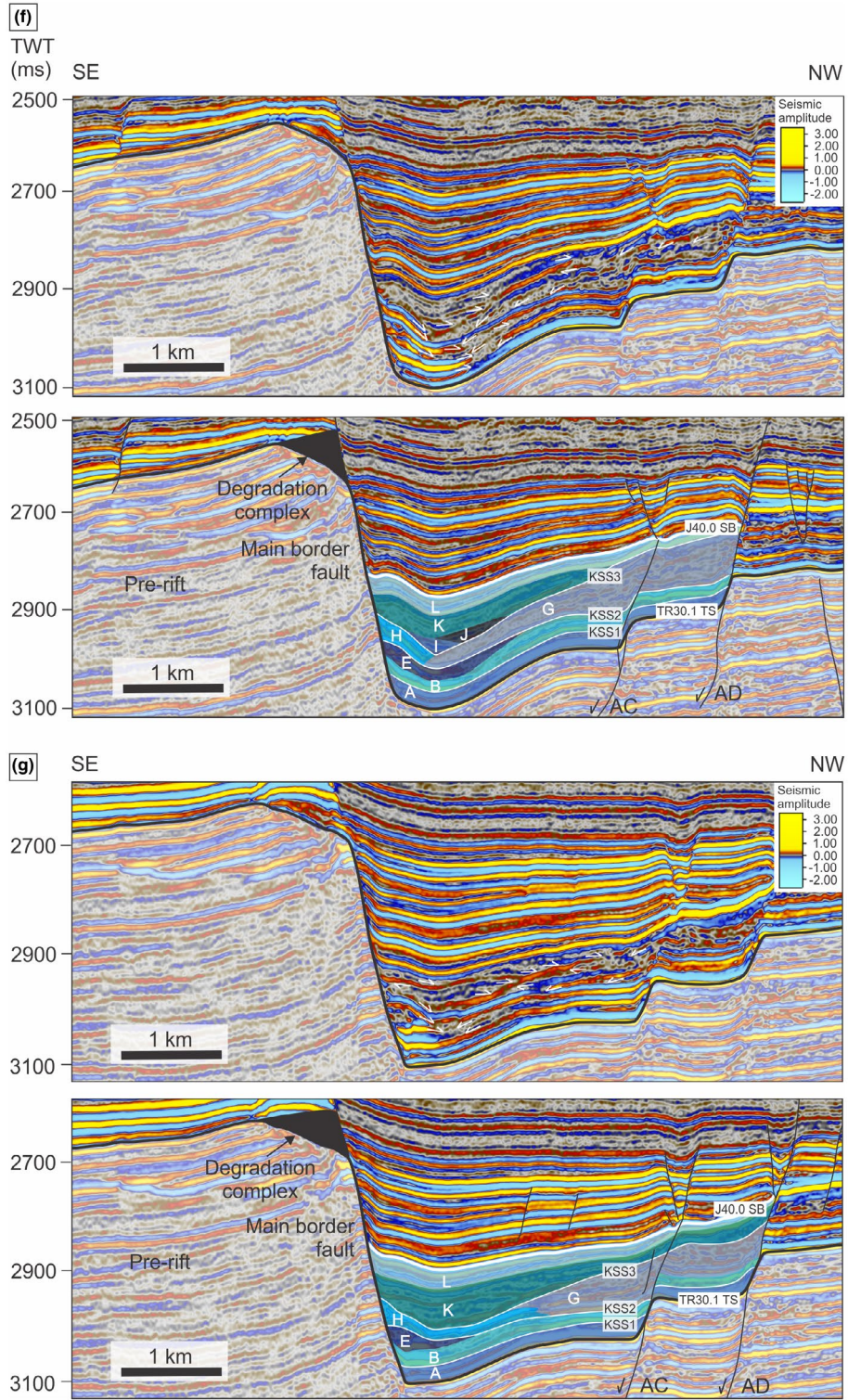


FIGURE 9 Continued

6.1.4 | Unit set 4

Unit Set 4 comprises Units I-L. The unit set is bounded by KSS3 at the base and the J40.0 SB at the top (Figures 9 and 10). Unit I is present in the central and northern sub-basins (Figure 9b). In the central sub-basin, it is downlapped and

overlain by Unit J, and fills the topography formed by underlying units (i.e. Units G and H; Figure 9c,d,f). Unit I comprises possible turbidites and pelagic/hemipelagic fall-out, deposited in a relatively deep water environment (SF4, Table 1).

In the most northerly part of the central sub-basin, the top of Unit J is defined by J40.0 SB (Figure 9c,d), whereas in the

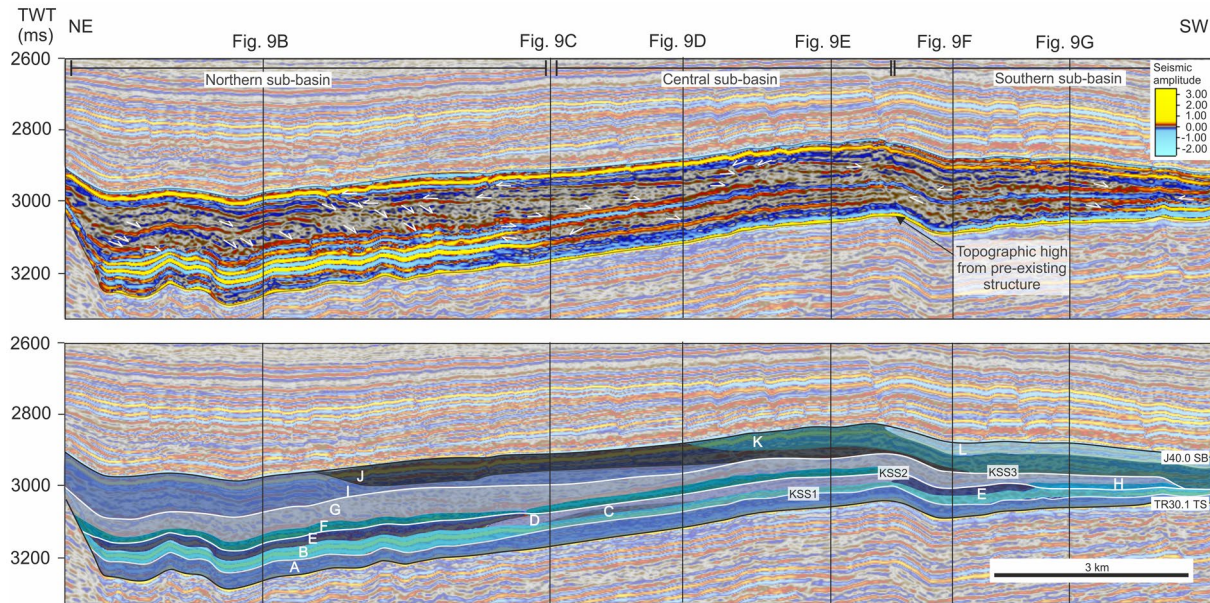


FIGURE 10 Representative strike section (NE-SW) through the hangingwall stratigraphy showing observations (upper) and interpretations (lower). The stratigraphic framework is shaded in blues (Units A-L). Key stratal surfaces (KSS1-3) are highlighted with white lines. Pre-rift stratigraphy is shaded white. Position of section is indicated in Figure 9a and is proximal to the Thebe-2 fault. Positions of Figure 9 dip sections, sub-basin extent and position of topographic high between the central and southern sub-basins are indicated. Uninterpreted section is available in the Appendix

southern part of the central sub-basin the unit is downlapped by Unit K (Figure 9e,f). Unit J comprises a thickened area (~2.5 km radius) positioned at the centre of the Thebe-2 fault and that downlaps underlying topography (e.g. Figure 9d). Dipping reflections extend ~800 m away from the centre of the Thebe-2 fault in Quadrant 6 (100 ms, 116 m high), where most footwall scarp degradation is observed and are interpreted to be slope apron deposits (SF1a, Table 1), or submarine fan deposits where they dip less steeply (SF4, Table 1). Elsewhere, the unit onlaps pre-existing topography through passive infilling of the basin.

Unit K is mostly limited to the southern sub-basin and is characterized by possible deep water deposits (SF4 and SF5, Table 1). Reflections dip gently from the NW and SE, downlapping Units G, I and J (Figure 9e-g).

Unit L is only present in the southern sub-basin and the top of Unit L is defined by J40.0 SB (Figure 9f,g). The unit has a maximum thickness of 80 ms, where it fills pre-existing lows in topography and is characterized by deep water deposits (SF4, Table 1).

6.2 | Along-strike variability of hangingwall fans

Footwall-, hangingwall- and axial-derived fans, interpreted as fan deltas, slope aprons and submarine fans (Figure 1), are

identified in the hangingwall basin, based upon the relative dip of related seismic reflections and their overall 3D geometries. Hangingwall-derived fans refer to those sourced from the hangingwall dip-slope (from the NW). These range in geometry and stacking pattern from aggradational clinoforms with distinct topsets (SF3, Table 1) in the southern sub-basin (Unit G, Figure 9f), to progradational foresets with limited topset development (SF2, Table 1) in the central sub-basin (Unit G, Figure 9e). Axial-derived fans (clinoforms) also mostly lack topsets, have lower foreset heights (20–40 ms; 23–46 m), and occur in two, vertically stacked packages that are internally defined by strongly progradational stacking (Table 1; Figure 11e,f).

Substantial variability is observed between footwall-derived fans that prograde away from the Thebe-2 fault. More specifically, four along-strike variations are observed: 1) overall 3D geometry, 2) the change in 3D geometry through time, 3) internal character, and 4) stacking patterns.

The overall 3D geometry of the fans varies along-strike and is used to distinguish SF1a (planar-slightly concave slope, interpreted to be slope aprons) from SF1b (clinoformal shape with clear topsets and foresets, interpreted to be fan deltas; Table 1). Both geometries appear to have developed during the deposition of Units E and H (Figure 12). Interfan areas (Figure 11c; position II, Figure 12a; Barrett, Gawthorpe, et al., 2019) exhibit concave reflections, as opposed to the sloping or convex to clinoformal shapes of the flanking fans.

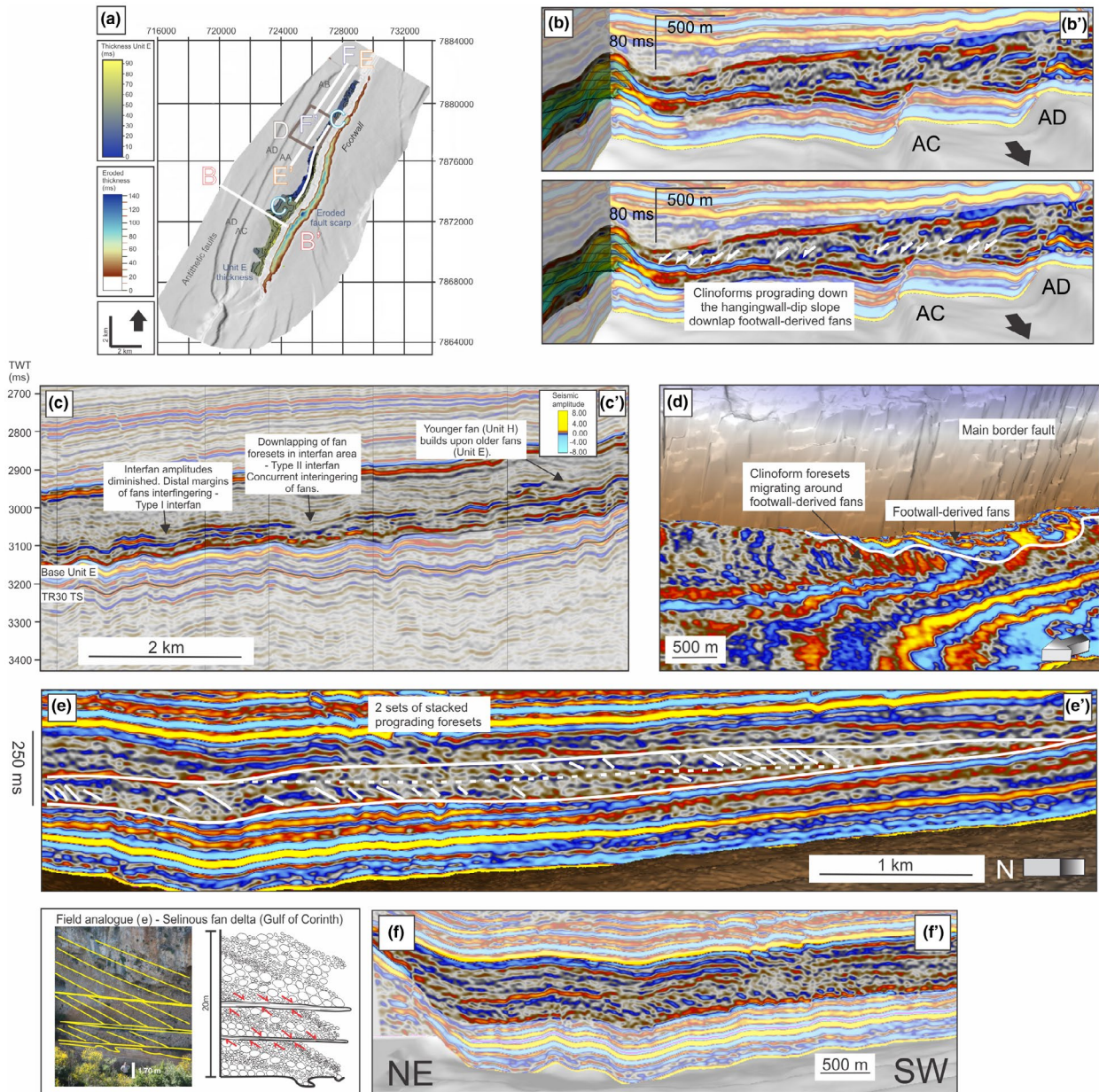


FIGURE 11 Architectural variability and geometric relationships between depositional systems across the basin. (a) Map of the basin with positions of sub-plots. (b) Clinoforms prograding down the hangingwall dip-slope and downlapping footwall-derived fan margins. (c) Strike section through footwall-derived fans showing interfan variability (interfan scheme according to Barrett, et al., 2019). (d) Amplitude time-slice to show axial-derived foresets migrating around footwall-derived fans. (e) Cross-section to show two sets of axial-derived, stacked foresets that prograded from NE fault tip. Field analogue of (e) from the Selinous fan delta (Gulf of Corinth, Greece) is highlighted (Barrett, Gawthorpe, et al., 2019). (f) Alternative, clean cross-section to show foresets prograding from NE fault tip. Uninterpreted versions of the seismic sections are available in the Appendix

The evolution of the fans through time commonly results in a change in their 3D geometry. Small, isolated fans (~40 ms; 46 m foreset height) are observed in Unit Set 1, which built away from the footwall of the Thebe-2 fault. In Unit Sets 2 and 3, individual fans enlarge (e.g. ~250 m radius; ~114 m foreset heights) and coalesce, occupying ~90% of the Thebe-2 fault length. Slope apron deposits develop between the fans (e.g. positions III, IV, V and VI, Figure 12a). Towards the northern end of the fault, fan size does not increase through time.

Positions III, IV, VI, IX and XI (Figure 12a,b) show a change from a clinoformal geometry in the lower units to a sloping geometry in Units E and H. The only position that maintains its clinoformal geometry throughout its development is position VII (Figure 12a,b).

The internal seismic character of the fans, in particular reflection continuity, is also variable *along-strike* from chaotic (e.g., positions IV and V, Figure 12a), through discontinuous (e.g., positions X and XI, Figure 12a), to continuous

(e.g., positions I, VI, IX and VIII, Figure 12a). The seismic character is also variable through *time*. For example, at position VII (Figure 12a), reflectivity is continuous towards the base, discontinuous in the middle, chaotic within a short interval, before becoming continuous again towards the top (Figure 12b). This could indicate variability in the deposit type as a result of different processes. For example, chaotic reflections on clinoform foresets could be indicative of mass transport deposits (mass-wasting) or small-scale faults, whereas the more continuous reflections could represent turbidites and intervening suspension settling-related deposits.

In the lower units, stacking patterns of clinoforms change from progradational towards the north-eastern fault tip (position I, Figure 12a) to aggradational towards the fault centre (position VI, Figure 12a). At position VII, where a clinoform-like geometry is maintained, stacking varies between progradational, aggradational and retrogradational trends through time (Figure 12b). This variability likely reflects the delicate balance between accommodation creation and sediment supply.

6.3 | Footwall analysis results

The most accurate estimation of fault throw is presented with measurements from the projected footwall cut-off (red line, Figure 13a), although there is some uncertainty with the mapping of the pseudo-surface. As the fault crest was eroded, any fault throw measurements using the highest point on the preserved fault scarp represent minimum values, hence we name this measurement the 'minimum fault throw' (grey line, Figure 13a). Both show a parabolic trend along-strike. Maximum fault throw (projected) is measured towards the fault centre (642 ms; 745 m), decreasing to c. 170 ms (197 m) towards the fault tips. Measurements do not reach the fault tips because the north-eastern fault tip is beyond the seismic dataset limit, and in the south-west, the fault extends into a relay zone with an adjacent fault and the fault tip position is obscured. A fault throw minimum is observed in Q7 (Figures 7 and 13), which coincides with a topographic high in the hangingwall that separates the central and southern sub-basins (Figure 10). The high appears to be inherited from an underlying, perpendicular structure. The fault throw minima suggests that this position could represent a now-breached early relay zone, which is supported by the bend in the fault trace at that position.

Minimum values of vertical erosion are apparent towards the fault tips (23 ms; 24 m using a velocity of 2066 m/s), increasing towards the fault centre with an approximate parabolic distribution along-strike, in line with fault throw. The maximum vertical erosion (228 ms; 236 m) is in Q6 (Figures 7 and 13a); this coincides with maximum headward erosion (905 m). Headward erosion is highly irregular along-strike, with large differences between peaks and

troughs over short distances. Notable peaks in headward erosion occur in Q3 and Q5-7 (Figure 13a). Nonetheless, there is still also an overall parabolic trend along the fault, in line with fault throw. Drainage systems in the footwall could be indicated by positions of high headward erosion, but distinct thalwegs, such as those documented in Elliott et al. (2012) were not clear in the seismic reflection data. Moreover, beyond the fault scarp degradation complex, the hangingwall dip slope is conformable until the next across-strike fault, thus an erosional landscape beyond the footwall crest is not apparent; either it did not form, or it was not preserved. However, observed fan deltas should have a sub-aerial source. This highlights the requirement for an alternative method to identify fixed, through-going sediment input points, if such features exist.

6.4 | Volume balancing - V_{HW}/V_{FW}

Volume balancing between the footwall-derived material in the hangingwall fans (V_{HW} of Units E and H) and the eroded material from the footwall (V_{FW}) reveals the position of through-going sediment input points, and areas of sediment bypass and/or redistribution. More specifically, quadrants that exhibit excess footwall erosion relative to hangingwall-fill ($V_{HW}/V_{FW} < 1$) represent areas of sediment bypass, and those that exhibit excess hangingwall-fill ($V_{HW}/V_{FW} > 1$) correspond to through-going, antecedent sediment input points. In the V_{HW}/V_{FW} plot (Figure 13b), many of the quadrants show values close to 1, indicating an approximate balance between erosion and adjacent sedimentation. In the $V_{HW} - V_{FW}$ plot, balanced quadrants have a value close to 0. Using both plots, the only area of convincing sediment bypass is in Q5, which coincides with an area characterized by the deposition of hangingwall slope aprons (Figure 12). Areas with apparent sediment bypass may in fact be balanced if smaller fans in other units were included in the hangingwall volume calculation.

The highest peak in V_{HW}/V_{FW} and $V_{HW} - V_{FW}$ occurs in Q6 ($V_{HW}/V_{FW} = 1.7$; Figure 13b,c), which could indicate the position of a through-going input point. This position coincides with the highest measured headward and vertical erosion along the fault. The fan in Q6 shows clinoforms in Unit Set 1 and slope apron geometries in Unit Sets 2–3 (position VI, Figure 12). A second major positive peak occurs in Q7 ($V_{HW}/V_{FW} = 1.5$; Figure 13b,c). This is coincident with highs in vertical and headward erosion, a fault throw minimum (Figure 13a), and a topographic high in the hangingwall basin (Figure 10). This peak also occurs where sustained clinoform development is apparent throughout Unit Sets 1–3, with clinoforms defined by clear topsets and radial foresets (SF1b, Table 1; position VII, Figure 12). Another peak, in Q3 ($V_{HW}/V_{FW} = 1.6$; Figure 13b) coincides with clinoform

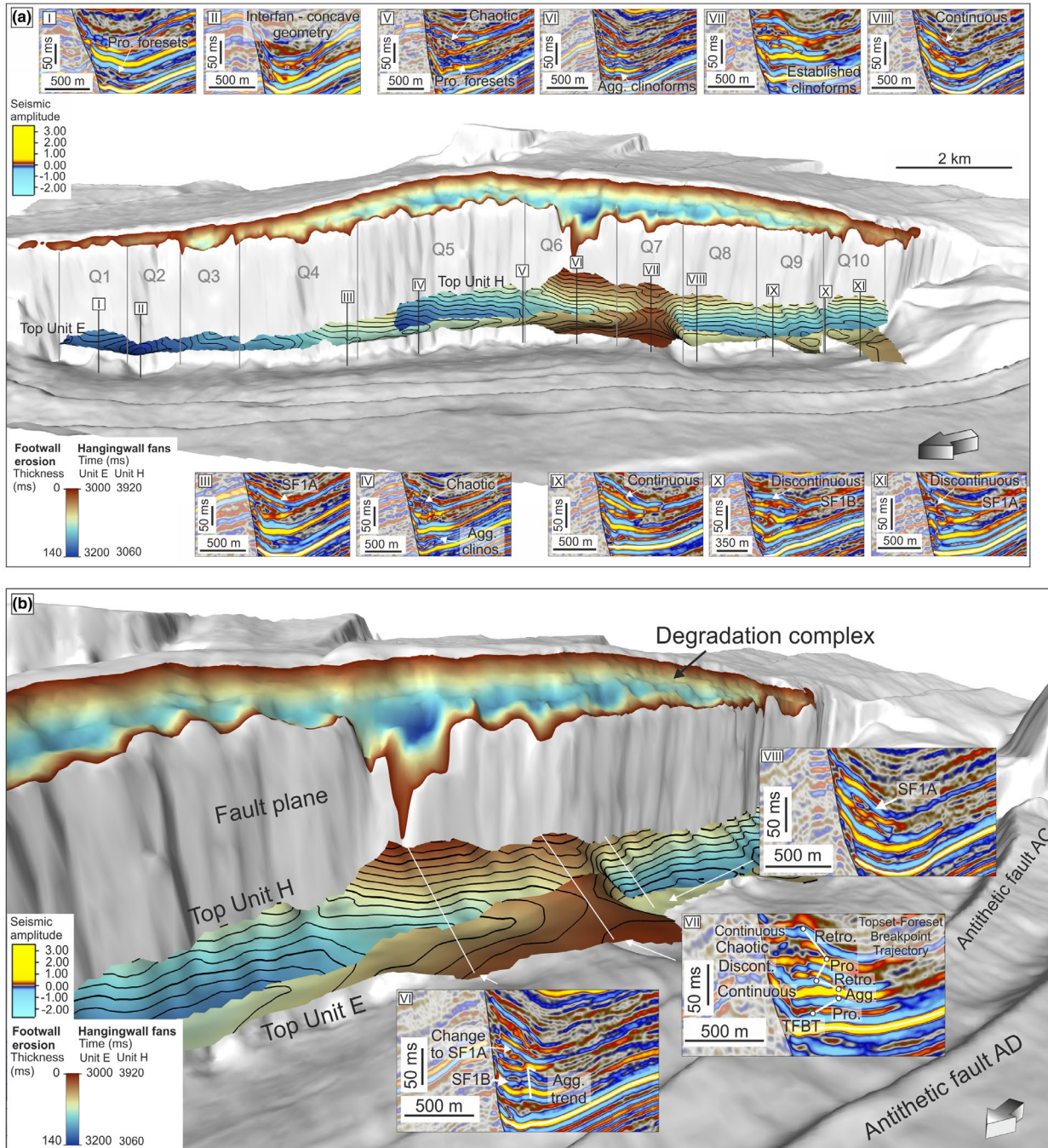


FIGURE 12 Along-strike variability of footwall-derived fans. (a) Top surfaces of Units E and H in the hangingwall are presented with the thickness of fault scarp erosion overlain onto the footwall. Positions I–XI show the substantial variability in fan character and geometry along the fault. Quadrants 1–10 are highlighted. (b) Focus upon three positions (VI–VIII) to show internal variability and stacking within the fans through the vertical succession. Continuous, discontinuous and chaotic labels refer to reflectivity. TFBT, Topset-Foreset Breakpoint Trajectory. Eroded thickness colour map from Crameri (2018)

development in the hangingwall in Unit Sets 1–2 (Figure 14). This peak does not correlate with peaks in headward and vertical erosion, but such highs occur in the adjacent Q2. One hypothesis may be that fans prograded obliquely from Q2 to Q3, an interpretation that is supported by the fan in Unit

E being skewed towards the NE (Top Unit E contour map, Figure 12a).

As previously discussed, our volume balancing approach underestimates hangingwall cell volume compared to footwall cell volume by up to 15%. This means any ratio value is

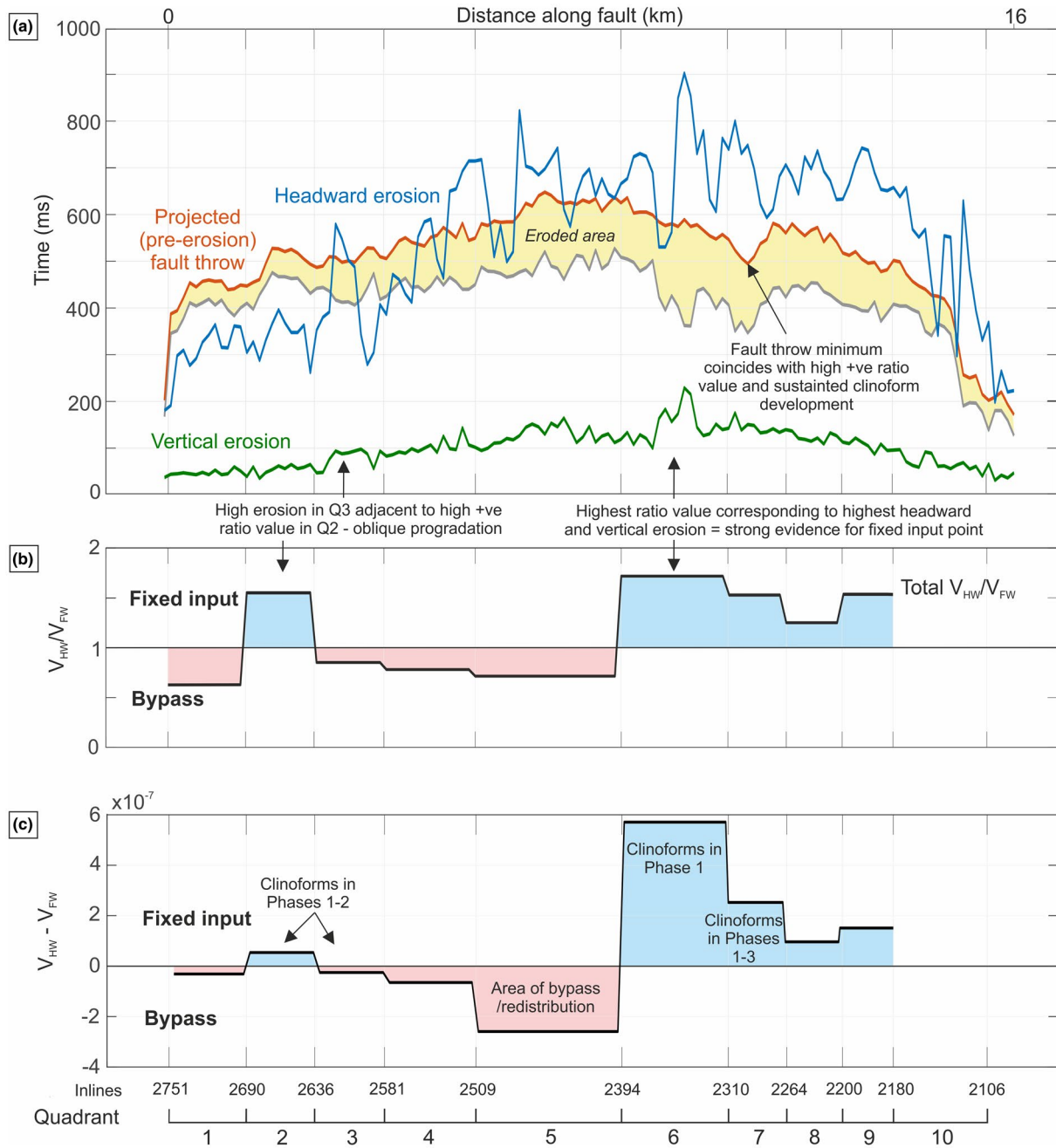


FIGURE 13 Graphs to show results of the footwall analysis and volume balancing. (a) Fault throw from the restored footwall (red) and from the preserved state of the fault (grey). Yellow shaded area represents amount of vertical erosion, which is also plotted in green. Vertical (green) and headward erosion (blue) vary along-strike but generally follow the parabolic trend of the fault throw distribution. (b) Ratio of hangingwall-fill of footwall-derived fans to footwall erosion (V_{HW}/V_{FW}). Values below 1 represent excess footwall erosion, i.e. areas of sediment bypass. Values greater than 1 represent areas of excess hangingwall-fill, i.e. positions of through-going sediment input points. (c) Plot to show $V_{HW} - V_{FW}$, which accounts for quadrant size. The largest positive ratio peak is in Quadrant 6, which coincides with the highest values of headward and vertical erosion, and clinoform development in Phase 1. The high, positive ratio value in Quadrant 7 coincides with the fault throw minimum and clinoform development in Phases 1–3. High headward and vertical erosion in Q3 occurs adjacent to a high positive ratio value in Q2, which suggests oblique progradation. This is confirmed with seismic mapping, e.g. Top Unit E contours in Figure 12a

a minimum estimate. As such, it is possible that areas characterized by excess erosion ($V_{HW}/V_{FW} < 1$) may be closer to a balance, and areas characterized by excess hangingwall-fill

($V_{HW}/V_{FW} > 1$) are underestimated. This supports our interpretation that Q3, Q6 and Q7 were defined by through-going sediment dispersal systems.

7 | TECTONO-STRATIGRAPHIC EVOLUTION

7.1 | Phase 1 – unit set 1

Thickening of Unit Set 1 strata into the Thebe-2 fault suggests that the fault became active at this time (Figure 9b–e and Figure 14). The pre-existing E–W (transverse) drainage that existed prior to faulting persists, which is reflected in some discrete distributary channel patterns in Unit A (SF6, Table 1). Small, footwall-derived fan deltas began to build at discrete locations along the Thebe-2 fault (Figure 14), as evidenced by the development of clinoforms (Figure 9b,d and Figure 12d). Small foreset heights in Unit Set 1 suggests relatively shallow water depths during fan delta development at this time. The progradational stacking of the fan deltas towards the north-eastern fault tip (Q3, Figure 14) suggests that sediment supply outpaced accommodation creation in the hangingwall. Conversely, aggradational stacking of the fan deltas towards the fault centre (Q6, Figure 14; position IV, Figure 12a) implies that sediment supply and accommodation creation were approximately equivalent. For a given sediment supply, this stacking distribution is typical of hangingwall basins where fault-related subsidence presents a parabolic distribution along-strike, with maximum subsidence towards the fault centre and minima at the fault tips (Childs, Nicol, Walsh, & Watterson, 2003; Dawers & Anderson, 1995; Gawthorpe et al., 1994; Gawthorpe, Hardy, & Ritchie, 2003; Hardy & Gawthorpe, 1998; Hunt & Gawthorpe, 2000; Jackson, Gawthorpe, Carr, & Sharp, 2005; Serck & Braathen, 2019; Walsh & Watterson, 1988). In Q7, the fan delta presents a progradational geometry (position VII, Figure 12b) despite being relatively close to the centre of the final fault length, either suggesting enhanced sediment supply and/or reduced accommodation creation at this position. The fan delta is positioned at a structural high defining the boundary between the central and southern sub-basins (Figure 9a). Here, a fault throw minimum (Figure 13a) and bend in the fault trace are interpreted to represent a breached relay, indicating low rates of subsidence and accommodation creation during the early stages of fault development. Sediment input may also have been focussed through the relay zone at this time (Densmore, Dawers, Gupta, Allen, & Gilpin, 2003; Fossen & Rotevatn, 2016; Gawthorpe & Hurst, 1993; Gupta, Underhill, Sharp, & Gawthorpe, 1999; Leeder & Jackson, 1993). This sediment input then became fixed in the landscape and continued to supply sediment throughout the basin evolution.

7.2 | Phase 2 – unit set 2

Unit Set 2 strata dip and start to thicken towards antithetic faults AB and AC (Figure 9b–g), which suggests that these faults became active at this time (Figure 14). Footwall-derived

fans continued to aggrade in the immediate hangingwall of the Thebe-2 fault, but their geometry changed. For example, the earlier (Unit Set 1) fan delta in Q6 was overlain by slope apron deposits (SF1a, Table 1; position VI, Figure 12b); this implies basin deepening, which is likely a result of increased fault-related subsidence. In the northern sub-basin (Q3) and at the structural high between the central and southern sub-basins (Q7), two fan deltas continued to build, suggesting increased sediment supply relative to accommodation creation at these specific locations (Figure 12). Fan delta stacking patterns in Q7 changed from progradational to aggradational-retrogradational at this time (position VII, Figure 12b), suggesting reduced sediment supply relative to accommodation creation, compared to that characterizing Phase 1. Hangingwall-derived, submarine fans prograded from antithetic faults AB and AC, and interfingered at their distal margin with footwall-derived fans from the Thebe-2 fault (Figure 11b and Figure 12). The fault scarp was at least partially subaerially exposed at this time, facilitating clinoform development and fault scarp degradation (Figure 6), which was greatest at the fault centre and least at the fault tips (Figures 5 and 13a). This pattern of erosion reflects the present distribution of slip and throw on the basin-bounding fault (Figure 13a). Antithetic fault crests lack seismic-scale erosion and are interpreted to be submerged (Figure 9). An alternative interpretation could be that the fault-offsets were levelled by deposition, but in that case, one would expect to see clinoforms building in a filled basin, rather than planar geometries indicative of submarine fans in an underfilled basin.

7.3 | Phase 3 – unit set 3

Fault-scarp degradation along the Thebe-2 fault continued, feeding hangingwall slope aprons and submarine fans (Figures 12 and 14). The through-going, fixed sediment input persisted in Q7, as the fan delta underwent a period of progradation before retrogradation (position VII, Figure 12b). Progradation could reflect an increased sediment supply relative to accommodation creation. An eventual return to the general retrogradational trend characterizing other along-strike locations likely reflects an increase in fault-related subsidence relative to sediment supply. Strata thicken into antithetic faults AA and AD at this time (Figure 9b–g), implying that they had become active. At the structural high between the central and southern sub-basins (Figure 9a), a hangingwall-derived fan delta prograded from antithetic fault AD, towards the SE. The fan delta downlapped onto and prograded up the distal margin of the NW-prograding, footwall-derived fan delta in Q7 (Figures 11b and 14). During this phase, the footwall-derived fan delta in Q3 was drowned and became

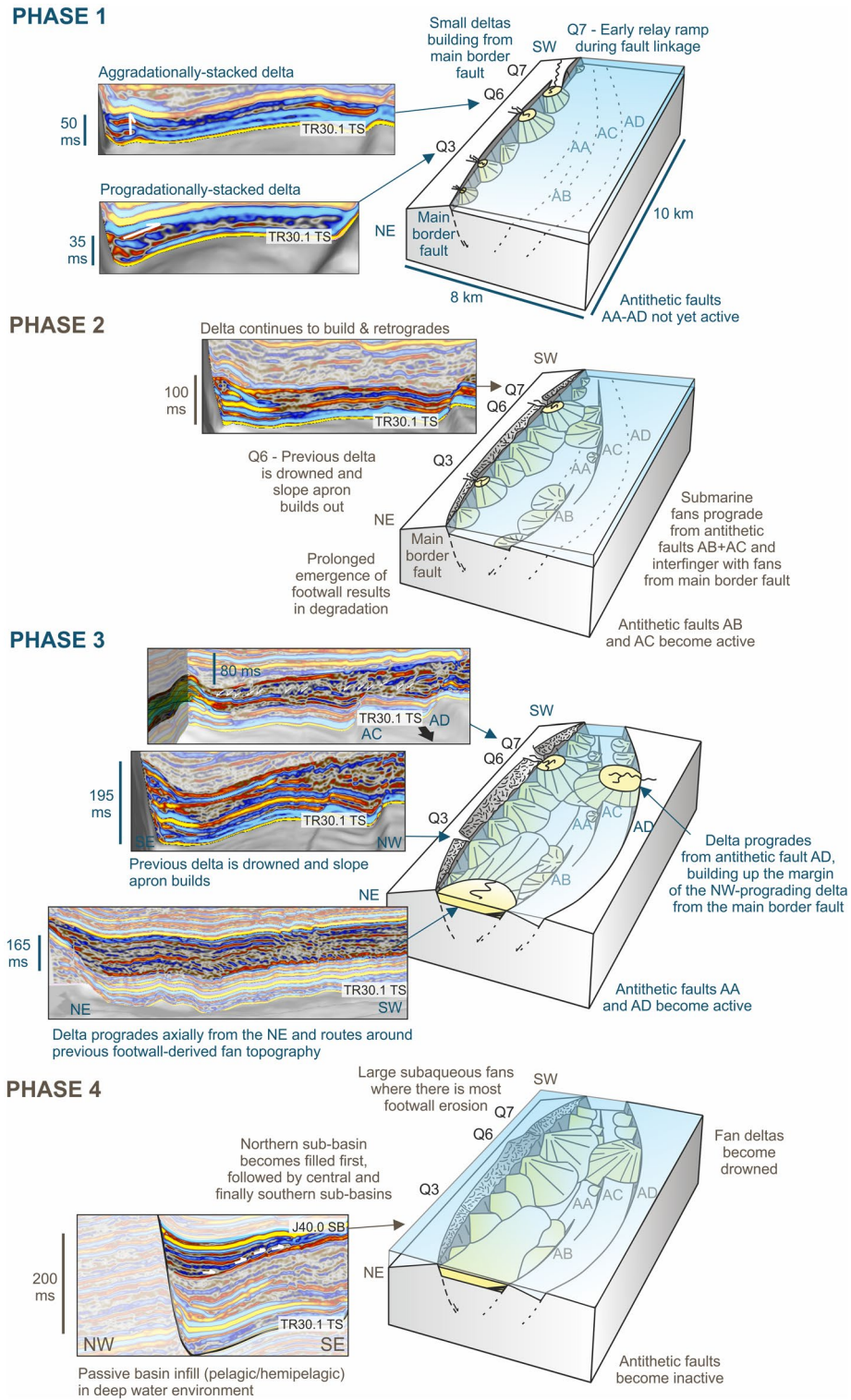


FIGURE 14 Block models to show the tectono-sedimentary evolution of the basin through Phases 1–4. Representative seismic extracts are shown to highlight evidence for interpretations. Antithetic faults AA-AD are indicated

a slope apron. Axial drainage from near the northern fault tip, parallel to the fault, then dominated sediment dispersal (Figure 11d–f). Strongly progradational clinofolds suggest a deltaic origin with a high sediment supply. These prograded around topography related to preceding and

concurrent footwall-derived deposits (Figure 11d). Two sets of stacked foresets are observed, separated by flat-lying reflections that are tentatively interpreted to represent flooding surfaces formed during two minor relative sea level cycles (Figure 11e).

7.4 | Phase 4 – unit set 4

Footwall-derived slope apron deposits continued to be locally deposited during Phase 4 (Figures 9d and 14, particularly at Q6, basinward of the area of greatest footwall degradation (position VI, Figure 12b). The absence of clinoforms suggests that the fan delta in Q7 was drowned (Figure 12). Elsewhere, lower angle dips and multiple onlaps in various directions indicate passive infilling of the basin (Figures 9 and 14), most likely be pelagic or hemipelagic sediment. The depositional environment at this time is unclear, but given the absence of clinoformal geometries that are otherwise indicative of a marginal setting, and the presence of slope apron deposits against the Thebe-2 fault, it is speculated to be a deeper water basin than in Phases 1–3. The lack of thickness changes across the antithetic faults suggest that they were no longer active. Across-fault offsets in the higher stratigraphy and minor thickening suggests continued but reduced activity on the Thebe-2 fault after the J40.0 SB.

8 | DISCUSSION

Through analysis of syn-rift footwall erosion and hanging-wall-fill, we have identified the positions of potential through-going sediment input points and have some constraint of the catchment history from the fault footwall. Moreover, we have assessed the contribution of sediment sources from other positions in the basin (hangingwall- and axial-derived), and the along-strike variability of their deposits through time. Here, we discuss the implications of these outcomes for: 1) footwall catchment identification in rifts and, 2) sediment supply to rift basins.

8.1 | Where are the footwall catchments?

We undertook a novel, volume balancing approach to identify whether sediment was sourced solely from footwall degradation, or whether intra-basin catchments were also important. We found excess hangingwall-fill ($V_{HW} > V_{FW}$), which suggests that fault scarp degradation was not the only sediment source. Using the ratio and difference between the two (V_{HW}/V_{FW} and $V_{HW}-V_{FW}$) for geometrically defined quadrants along the fault, we could more precisely constrain the areas that were dominated by sediment bypass ($V_{HW} < V_{FW}$) and the areas that coincide with potential fixed, through-going sediment input points ($V_{HW} > V_{FW}$).

Excess hangingwall-fill was highlighted in Q3, 6 and 7, as the positions of potential through-going sediment input points and thus, catchments beyond the fault crest. Q7 coincides with the topographic high between the central and southern sub-basins, a fault throw minimum, peaks in vertical

and headward erosion, and sustained clinoform development in the immediate hangingwall through Phases 1–3. It is interpreted that sediments entered the basin here through an early relay zone (Phase 1) that was later breached, yet continued to be a focal basin entry point (Phase 2–3; e.g. Cowie, Gupta, & Dawers, 2000; Young, Gawthorpe, & Sharp, 2002). In Q3 and 6, early clinoforms in the hangingwall were overlain by slope apron deposits. Q6 is characterized by the highest headward and vertical erosion. Q3 is suggested to be fed obliquely by high erosion in Q2. It was not possible to constrain the timing of erosion relative to hangingwall sedimentation from the volume-balancing approach alone. Seismic mapping of clinoforms and planar-sloping reflectors in the hangingwall stratigraphy can resolve deltaic versus slope apron deposits, and formed the basis of the relative timing interpretation (Figure 14). Our interpretations suggest that through-going sediment inputs switched off (sediment supply reduced) in various phases (Figure 14), which could have resulted from slope changes associated to fault growth (e.g. Attal, Tucker, Whittaker, Cowie, & Roberts, 2008; Cowie et al., 2006). It is also possible that the transition from fan delta to slope apron deposits in the hangingwall did not occur from the switching-off of sediment inputs, but was the result of subsidence rate increasing and outpacing the sediment supply.

The Thebe-2 sub-basin was (and still is) located in a relatively distal position on the Exmouth Plateau basin. Regional stratigraphic analysis reports an overall increase in water depth from the Late Triassic to the Late Jurassic (Hocking et al., 1988; Longley et al., 2002; Marshall & Lang, 2013). Although we have no constraints on the precise timing of the basin fill, our volume balancing approach and observations of fault-scarp degradation and hangingwall clinoform development suggests: 1) a relatively shallow water environment, 2) exposure of the footwall crest, and 3) the presence of palaeo-coastlines against the Thebe-2 fault during Phases 1–3, and against antithetic fault AD during Phase 3. In Phase 4, these sources were flooded as relative sea-level rose.

We refer to local well data to help further constrain our interpretation of depositional environment and water depth in the footwall and hangingwall of the Thebe-2 fault block. No local wells penetrate the hangingwall stratigraphy, being positioned on footwall or horst-block highs. The well data in the footwall of the Thebe-2 fault block (Thebe-2 well) does not provide direct evidence of subaerial exposure (e.g. palaeosols), containing only a condensed (2–3 m) interval of claystones. The well does not penetrate the degraded area of the fault scarp and is positioned 2.5 km away from the nearest hangingwall coastline, inferred from the location of hangingwall dip-slope clinoforms. The timing of claystone deposition at the well is unknown. It could have occurred in the later syn-rift phase, after subaerial exposure and when a submarine setting is inferred from hangingwall deposits against the Thebe-2 fault, transitioning from fan deltas to slope aprons. Completion reports from other local

wells (Thebe-1, Kentish Knock-1, Cadwallon-1, Genseric-1, Blake-1), which are drilled on footwall highs, present interpretations of brackish-shelfal marine environments for the equivalent Brigadier, Murat and Athol formations (Ellis, 2010a; Ellis et al., 2008; Forster, 2016; Monro, 2012; Taylor, 2012). The recent Blake-1 well contains a 39 m-thick, brackish water interval, which palynological analysis reveal are in fact Pliensbachian (Murat Siltstone) based on the presence of a rare spinose *A Micrhystridium spp.* This interval is overlain by Callovian shelfal deposits (Athol Formation; Forster, 2016). The Kentish Knock-1 well also contains glauconite-bearing, nearshore-to-brackish claystone, which is assigned to the Athol Formation (Ellis, 2010a). In the Arnhem-1 well, an intra-Jurassic unconformity is documented between the Brigadier and Athol formations (Allen et al., 2013). The Murat and Athol formations are absent in the Genseric-1 and Cadwallon-1 wells (Monro, 2012; Taylor, 2012), and the syn-rift interval is faulted out in Dalia South-1 (Sturrock, 2011). Bilal et al. (2018) argue for degradation in a subaqueous environment, based on the absence of subaerial indicators in other local well data and submarine canyon development. However, no previous reporting highlights or provides a mechanistic explanation for clinoform development and footwall crest degradation of this scale in a fully marine setting, in the absence of a subaerial source. Moreover, the relatively shallow water environment encountered some nearby wells and unconformity in others, suggests that localized subaerial exposure is not unlikely.

Our interpretation is consistent with large-scale, palaeogeographic maps from the J30 sequence (Longley et al., 2002) that show deposition in narrow rift valleys and palaeo-coastlines fringing exposed fault blocks. Similar scenarios of uplifted and exposed footwall highs and islands supplying hangingwall basins are interpreted in the Late Jurassic North Sea (Berger & Roberts, 1999; McArthur, Jolley, Hartley, Archer, & Lawrence, 2016; Nøttvedt et al., 2000; Roberts, Kuszniir, Yielding, & Beeley, 2019; Yielding, Badley, & Roberts, 1992) and the Quaternary-modern Aegean Sea (Papadopoulos & Pavlides, 1992; Stiros et al., 1994).

8.2 | Sediment supply in rift basins

The volume of sediment in Units E and H amounts to ~10% of the total hangingwall-fill. Footwall-derived material is apparent in other units, so this is a minimum estimate of footwall-derived material in the hangingwall basin. However, the hangingwall- and axial-derived systems (and pelagic and hemipelagic material) made a clear and substantial contribution to the basin-fill (<90%), and their relative influence changed through time as the basin evolved. During the early stages of fault activity and basin development, footwall-derived systems prograded basinward into newly formed accommodation. Later, footwall-derived

systems grew as fault activity and associated degradation increased, and changed in style along-strike according to the local ratio of accommodation creation to sediment supply. Individual antecedent systems also grew, as catchments were uplifted in the footwall, yielding greater sediment supply. Hangingwall-derived systems started to play an important role when antithetic faults became active. This is interpreted from a transition from approximately E-W oriented drainage in Unit set 1, as evidence by channels and NW-prograding fans, to the addition of SE-oriented drainage in Unit sets 2–3, as evidenced by fans in the thickened strata against the antithetic faults. The axial system, which prograded from the northern fault tip, formed a large component of Unit G, but no system prograded axially from the southern fault tip. The growth and interaction of adjacent faults outside of the immediate study area and local antithetic faults generated variable intra-basin relief and gradients, and are thus likely to have played a role in determining sediment flux, entry points, and the migration of depositional systems around the basin (Gawthorpe & Hurst, 1993; Jackson & Leeder, 1993; Ravnås & Steel, 1998; Roberts et al., 1993; Whittaker, Attal, & Allen, 2010).

Coeval and competing sediment supply systems result in complex process and architectural interactions and are an important aspect of tectono-sedimentary models for rifts. Here, depositional systems represent a spectrum of compensational stacking styles (e.g. Bell, Stevenson, Kane, Hodgson, & Poyatos-Moré, 2018; Mohrig, Heller, Paola, & Lyons, 2000; Olariu & Bhattacharya, 2006; Prélat, Hodgson, & Flint, 2009; Straub & Pyles, 2012; Wang, Straub, & Hajek, 2011), and are observed to interfinger, abruptly downlap, to build up the flanks of another, or to route around each other. The relative timing of establishment and progradation of different depositional systems clearly plays an important role in this interaction, but also the depositional gradients of the competing systems (Dodd, McCarthy, & Richards, 2018) and the individual stream power of, for example river systems, given it is this which strongly influences its ability to erode and/or bypass (Stevenson, Jackson, Hodgson, Hubbard, & Eggenhuisen, 2015). However, we note that the widely used conceptual models for the tectono-sedimentary evolution of rifts do not detail the stratal interactions between depositional systems of different origins (e.g. Gawthorpe & Leeder, 2000) and do not fully document the relative contribution of footwall-, hangingwall- and axial-derived sources. This study presents a rare example where all three systems contribute to the fill of the hangingwall depocenter. Such conceptual models should be adapted to incorporate contribution and interactions of various sediment entry points to the basin that this and other recent studies have highlighted (e.g. Cullen et al., 2019; Henstra et al., 2017; McArthur, Hartley, et al., 2016; Muravchik et al., 2018).

8.3 | Implications for hydrocarbon exploration

Hydrocarbon exploration across the Exmouth Plateau has largely targeted fluvial reservoirs within the Mungaroo Fm. in the footwall highs. We have demonstrated fault block crest degradation, which reduces the gross rock volume of such reservoirs. Detailed mapping is thus required to make accurate hydrocarbon volume and uncertainty estimates, and here we have constrained the variability of the degradation complex along-strike. Our interpretation of footwall exposure and observations of clinofolds in this outboard part of the Exmouth Plateau, also highlight reservoir potential in shallow and deep water fans in the hangingwall basins, such as those characterizing the Brae Play in the North Sea (Turner et al., 2018). We have documented styles of interaction between footwall-, hangingwall- and axial-derived depositional systems in the hangingwall basin, which are important when assessing the syn-rift play potential in rifts. These interactions ultimately define the distribution, connectivity, trapping and pinch-out geometries of reservoir and seal units.

Our quantitative volumetric approach could be applied to identify the position of through-going sediment input points here, and in other hydrocarbon-bearing rifts. These far-field sources yield sediment that has travelled further, and are thus likely to be more reworked and mature than sediment derived from the immediately adjacent fault scarp (Leppard & Gawthorpe, 2006; Reading & Richards, 1994; Richards et al., 1998). Therefore, when prospecting hangingwall fans, areas sourced by established catchments beyond the footwall crest could have higher reservoir quality and thus deliverability. The approach could be similarly used to identify areas dominated by sediment bypass (Stevenson et al., 2015); it could thus be a useful tool in the search for prospective subaqueous fans deposited further basinward, perhaps in the basin axis. Both approaches would ideally be performed with depth-converted seismic reflection data build from a well-constrained velocity model; this would allow for a more accurate estimate of eroded and deposited sediment volumes. However, as we demonstrate, it is still possible to estimate and work with the volume balance ratio derived from time-migrated seismic reflection data. Identification and mapping of footwall catchments and/or imaging of footwall-derived, hangingwall clinofolds supports the volume balancing approach. Here, footwall catchments beyond the fault crest were not imaged, but mapping hangingwall clinofolds was possible and validated the volume balance results. In areas where data quality restricts the imaging of footwall catchments or hangingwall clinofolds, volume balancing could be a pragmatic approach.

9 | CONCLUSION

A quantitatively-informed interpretation of the tectono-sedimentary evolution of the Thebe-2 fault block on the Exmouth Plateau, NW Shelf, offshore Australia, suggests that the Thebe-2 hangingwall basin evolved through four phases linked to the evolution of the Thebe-2 fault and a number of parallel, antithetic faults, which became active at different times. Through-going sediment input points were identified in Quadrants 3, 6 and 7. The latter persisted throughout the basin evolution and coincides with a topographic high between the central and southern sub-basins, a fault throw minimum, peaks in vertical and headward erosion, and convincing and sustained clinofold development in the immediate hangingwall. Exposure of the border fault footwall and inboard/adjacent fault terraces are interpreted to have produced small catchments that fed the hangingwall basin, reflecting deposition in narrow rift valleys and palaeo-shorelines that fringed emergent fault blocks in the outboard part of the Exmouth Plateau.

Overall there are two main outcomes of this study that represent advances in the fields of syn-rift geomorphology and tectono-stratigraphy:

1. Complex process and architectural interactions are observed between depositional systems within the same basin, but with different origins (footwall-, hangingwall- and axial-derived) that yield variable contributions to the hangingwall-fill through time. Depositional systems are observed to interfinger, abruptly downlap, build up the flanks of another, or route around each other, which represents a spectrum of compensational stacking styles within a fault-confined basin. This is an important outcome which should be incorporated into existing models for tectono-sedimentary development in rift basins.
2. A quantitative volume balancing approach is presented that could be used to independently locate through-going input points in other basins, particularly where preservation of erosional landscapes is limited and/or subsurface imaging is challenging. Similarly, it could be useful tool for identifying areas along a fault that were dominated by sediment bypass.

ACKNOWLEDGEMENTS

This work forms part of the PhD thesis of Bonita Barrett. The authors thank the project sponsor, Neptune Energy that sponsored the SMRG (Shallow Marine Research Group). Geoscience Australia is also thanked for the provision of publicly accessible subsurface data from the northern Carnarvon Basin, Australia, which is available for download from the NOPIMS (National Offshore Petroleum Information Management System) data repository website:

<https://nopims.dmp.wa.gov.au/nopims>. Catherine Skilliter is acknowledged for the regional maps used in this work. Petrel software was used for seismic mapping and gridding. Finally, we are grateful to Dora Marín, Awad Bilal and Rodmar Ravnås for providing thorough and constructive reviews of the manuscript, and whose contributions have greatly improved the quality of the paper.

CONFLICT OF INTEREST

None declared.

PEER REVIEW

The peer review history for this article is available at <https://publons.com/publon/10.1111/bre.12508>.

DATA AVAILABILITY STATEMENT

The data used in this study are publicly accessible from Geoscience Australia, and are available for download from the NOPIMS (National Offshore Petroleum Information Management System) data repository website: <https://nopims.dmp.wa.gov.au/nopims>.

ORCID

Bonita J. Barrett  <https://orcid.org/0000-0002-3274-822X>

David M. Hodgson  <https://orcid.org/0000-0003-3711-635X>

Christopher A.-L. Jackson  <https://orcid.org/0000-0002-8592-9032>

Christopher Lloyd  <https://orcid.org/0000-0001-5011-1284>

Richard E. Ll. Collier  <https://orcid.org/0000-0002-8001-0510>

REFERENCES

- Allen, P., Van der Aa, D., Rodger, S., & Ellis, C. (2013). *Arnhem-1 final well completion report, interpretive volume, WA-364-P (R1)*. Chevron Australia Pty Ltd.
- Alves, T. M., & Cupkovic, T. (2018). Footwall degradation styles and associated sedimentary facies distribution in SE Crete: Insights into tilt-block extensional basins on continental margins. *Sedimentary Geology*, 367, 1–19. <https://doi.org/10.1016/j.sedgeo.2018.02.001>
- Attal, M., Tucker, G. E., Whittaker, A. C., Cowie, P. A., & Roberts, G. P. (2008). Modeling fluvial incision and transient landscape evolution: Influence of dynamic channel adjustment. *Journal of Geophysical Research*, 113, F03013. <https://doi.org/10.1029/2007JF000893>
- Backert, N., Ford, M., & Malartre, F. (2010). Architecture and sedimentology of the Kerinitis Gilbert-type fan delta, Corinth Rift, Greece. *Sedimentology*, 57, 543–586. <https://doi.org/10.1111/j.1365-3091.2009.01105.x>
- Barrett, B. J., Collier, R. E. L., Hodgson, D. M., Gawthorpe, R. L., Dorrell, R. M., & Cullen, T. M. (2019). Quantifying faulting and base level controls on syn-rift sedimentation using stratigraphic architectures of coeval, adjacent Early-Middle Pleistocene fan deltas in Lake Corinth, Greece. *Basin Research*, 31(6), 1040–1065. <https://doi.org/10.1111/bre.12356>
- Barrett, B. J., Gawthorpe, R. L., Collier, R. E. L., Hodgson, D. M., & Cullen, T. M. (2019). Syn-rift deltaic interfan stratigraphy as archives of sedimentation and basin evolution. *The Depositional Record*, 6, 117–143.
- Barrett, B. J., Hodgson, D. M., Collier, R. E. L., & Dorrell, R. M. (2018). Novel 3D sequence stratigraphic numerical model for syn-rift basins: Analysing architectural responses to eustasy, sedimentation and tectonics. *Marine and Petroleum Geology*, 92, 270–284. <https://doi.org/10.1016/j.marpetgeo.2017.10.026>
- Bell, D., Stevenson, C., Kane, I., Hodgson, D. M., & Poyatos-Moré, M. (2018). Topographic controls on the development of contemporaneous but contrasting basin-floor depositional architectures. *Journal of Sedimentary Research*, 88, 1169–1189. <https://doi.org/10.2110/jsr.2018.58>
- Bentham, P., Collier, R. E. L., Gawthorpe, R. L., Leeder, M. R., & Stark, C. (1991). Tectono-sedimentary development of an extensional basin: The Neogene Megara Basin, Greece. *Journal of the Geological Society*, 148, 923–934. <https://doi.org/10.1144/gsjgs.148.5.0923>
- Berger, M., & Roberts, M. (1999). The Zeta Structure: A footwall degradation complex formed by gravity sliding on the western margin of the Tampen Spur, Northern North Sea. *Geological Society, London, Petroleum Geology Conference Series*, 5, 107–116. <https://doi.org/10.1144/0050107>
- Bilal, A., McClay, K., & Scarselli, N. (2018). Fault-scarp degradation in the central Exmouth Plateau North West Shelf, Australia. In K. R. McClay & J. A. Hammerstein (Eds.), *Passive margins: tectonics, sedimentation and magmatism*. *Geological Society, London, Special Publications*, 476(1), 231–257. <https://doi.org/10.1144/SP476.11>
- Bradshaw, M. T., Bradshaw, J., Murray, A. P., Needham, D. J., Spencer, L., Summons, R. E., ... Winn, S. (1994). Petroleum systems in west Australian basins. In P. G. Purcell & R. R. Purcell (Eds.), *The Sedimentary Basins of Western Australia: Proceedings of the Petroleum Exploration Society of Australia Symposium* (pp. 93–118). Perth: PESA.
- Bradshaw, M. T., Yeates, A. N., Beynon, R. M., Brakel, A. T., Langford, R. P., Totterdell, J. M., & Yeung, M. (1988). Palaeogeographic evolution of the North West Shelf region. In P. G. Purcell & R. R. Purcell (Eds.), *Proceedings of the North West Shelf Symposium* (pp. 29–54). Perth: PESA.
- Chen, H., Wood, L. J., & Gawthorpe, R. L. (2020). Sediment dispersal and redistributive processes in axial and transverse deep-time source-to-sink systems of marine rift basins: Dampier Sub-basin, Northwest Shelf, Australia. *Basin Research*, <https://doi.org/10.1111/bre.12462>
- Childs, C., Nicol, A., Walsh, J. J., & Watterson, J. (2003). The growth and propagation of synsedimentary faults. *Journal of Structural Geology*, 25, 633–648. [https://doi.org/10.1016/S0191-8141\(02\)00054-8](https://doi.org/10.1016/S0191-8141(02)00054-8)
- Collier, R. E. L., & Gawthorpe, R. L. (1995). Neotectonics, drainage and sedimentation in central Greece: Insights into coastal reservoir geometries in syn-rift sequences. *Geological Society, London, Special Publications*, 80, 165–181. <https://doi.org/10.1144/GSL.SP.1995.080.01.08>
- Cotterill, C. J. (2002). A high resolution Holocene fault activity history of the Aigion shelf, Gulf of Corinth, Greece. PhD Thesis, School of Ocean and Earth Sciences, University of Southampton, UK.

- Cowie, P. A., Attal, M., Tucker, G. E., Whittaker, A. C., Naylor, M., Ganas, A., & Roberts, G. P. (2006). Investigating the surface process response to fault interaction and linkage using a numerical modelling approach. *Basin Research*, *18*, 231–266. <https://doi.org/10.1111/j.1365-2117.2006.00298.x>
- Cowie, P. A., Gupta, S., & Dawers, N. H. (2000). Implications of fault array evolution for synrift depocenter development: Insights from a numerical fault growth model. *Basin Research*, *12*, 241–261.
- Crameri, F. (2018). Scientific colour maps: Perceptually uniform and colour-blind friendly. *Zenodo*. <https://doi.org/10.5281/zenodo.1243862>
- Cullen, T. M., Collier, R. E. L., Gawthorpe, R. L., Hodgson, D. M., & Barrett, B. J. (2019). Axial and transverse deep-water sediment supply to syn-rift fault terraces: Insights from the West Xylokaastro Fault Block, Gulf of Corinth, Greece. *Basin Research*, <https://doi.org/10.1111/bre.12416>
- Dart, C. J., Collier, R. E. L., Gawthorpe, R. L., Keller, J. V. A., & Nichols, G. (1994). Sequence stratigraphy of (?)Pliocene-quaternary synrift, gilbert-type fan deltas, Northern Peloponnesos, Greece. *Marine and Petroleum Geology*, *11*, 545–560. [https://doi.org/10.1016/0264-8172\(94\)90067-1](https://doi.org/10.1016/0264-8172(94)90067-1)
- Dawers, N. H., & Anderson, M. H. (1995). Displacement-length scaling and fault linkage. *Journal of Structural Geology*, *17*, 607–614. [https://doi.org/10.1016/0191-8141\(94\)00091-D](https://doi.org/10.1016/0191-8141(94)00091-D)
- Deng, H., & McClay, K. (2019). Tectono-stratigraphy of the Dampier sub-basin, North West Shelf of Australia. In K. R. McClay, J. A. Hammerstein (Eds.), *Passive margins: tectonics, sedimentation & magmatism. Geological Society, London, Special Publications*, *476*, SP476-2018–180. <https://doi.org/10.1144/SP476-2018-180>
- Densmore, A. L., Dawers, N. H., Gupta, S., Allen, P. A., & Gilpin, R. (2003). Landscape evolution at extensional relay zones. *Journal of Geophysical Research*, *108*, 2273. <https://doi.org/10.1029/2001JB001741>
- Dodd, T. J., McCarthy, D. J., & Richards, P. C. (2018). A depositional model for deep-lacustrine, partially-confined, turbidite fans: Early Cretaceous, North Falkland Basin. *Sedimentology*, *66*, 53–80. <https://doi.org/10.1111/sed.12483>
- Dorsey, R. J., & Umhoefer, P. J. (2000). Tectonic and eustatic controls on sequence stratigraphy of the Pliocene Loreto Basin, Baja California Sur, Mexico. *Geological Society of America Bulletin*, *112*, 177–199. [https://doi.org/10.1130/0016-7606\(2000\)112<177:TAECOS>2.0.CO;2](https://doi.org/10.1130/0016-7606(2000)112<177:TAECOS>2.0.CO;2)
- Dorsey, R. J., Umhoefer, P. J., & Renne, P. R. (1995). Rapid subsidence and stacked gilbert-type fan deltas, Pliocene Loreto Basin, Baja California Sur, Mexico. *Sedimentary Geology*, *98*, 181–204. [https://doi.org/10.1016/0037-0738\(95\)00032-4](https://doi.org/10.1016/0037-0738(95)00032-4)
- Elliott, G. M., Wilson, P., Jackson, C.-A.-L., Gawthorpe, R. L., Michelsen, L., & Sharp, I. (2012). The linkage between fault throw and footwall scarp erosion patterns: An example from the Bremstein Fault Complex, offshore Mid-Norway. *Basin Research*, *24*, 180–197. <https://doi.org/10.1111/j.1365-2117.2011.00524.x>
- Ellis, C. (2010a). *Kentish Knock-1 well completion report, interpretive volume, WA-365-P*. Chevron Australia Ply Ltd.
- Ellis, C. (2010b). *Guardian-1 well completion report, interpretive volume, WA-365-P*. Chevron Australia Ply Ltd.
- Ellis, C., Woodall, M., Goody, A., Lim, D., & Locke, M. (2008). *Thebe-1 and Thebe-1CH well completion report, interpretive volume, WA-346-P. BHP*. Billiton Petroleum Pty Ltd.
- Ellis, C., Woodall, M., Goody, A., Lim, D., & Locke, M. (2009a). *Thebe-2 and Thebe-2CH well completion report, basic data volume, WA-346-P. BHP*. Billiton Petroleum Pty Ltd.
- Ellis, C., Woodall, M., Goody, A., Lim, D., & Locke, M. (2009b). *Thebe-2 and Thebe-2CH well completion report, interpretive volume, WA-346-P. BHP*. Billiton Petroleum Pty Ltd.
- Etheridge, M. A., & O'Brien, G. W. (1994). Structural and tectonic evolution of the Western Australia margin system. *PESA Journal*, *22*, 45–63.
- Exon, N. F., Haq, B. U., & von Rad, U. (1992). Exmouth Plateau revisited: Scientific drilling and geological framework. *Proceedings of the Ocean Drilling Program, Scientific Results*, *122*, 3–20.
- Ford, M., Williams, E. A., Malartre, F., & Popescu, S. M. (2007). Stratigraphic architecture, sedimentology and structure of the Vouraikos Gilbert-type fan delta, Gulf of Corinth, Greece. In G. Nichols, E. Williams & C. Paola (Eds.), *Sedimentary processes, environments and basins. A tribute to peter friend. International Association of Sedimentologists Special Publications*, *38*, 49–90.
- Forman, D. J., & Wales, D. W. (1981). Geological evolution of the Canning Basin, Western Australia. *Bureau of Mineral Resources, Geology and Geophysics Bulletin*, *210*, 91.
- Forster, C. (2016). *Blake-1 final well completion report, WA-383-P*. Chevron Australia Ply Ltd.
- Fossen, H., & Rotevatn, A. (2016). Fault linkage and relay structures in extensional settings – a review. *Earth-Science Reviews*, *154*, 14–28. <https://doi.org/10.1016/j.earscirev.2015.11.014>
- Fraser, S. I., Robinson, A. M. et al (2002). Upper Jurassic. In A. Armour, D. Evans, & C. Hickey (Eds.), *The millenium atlas: petroleum geology of the central and Northern North Sea* (pp. 157–189). London: The Geological Society.
- Gartrell, A. P. (2010). Rheological controls on extensional styles and the structural evolution of the Northern Carnarvon Basin, North West Shelf, Australia. *Australian Journal of Earth Sciences*, *47*, 231–244.
- Gartrell, A. P., Keep, M., van der Reit, C., Paterniti, L., & Ban, S. (2019). *Variable inversion of polyphase rift basins impacts the Triassic sequence architecture of the NW Shelf, Australia*. San Antonio, TA: AAPG Convention and Exhibition.
- Gartrell, A. P., Torres, J., Dixon, M., & Keep, M. (2016). Mesozoic rift onset and its impact on the sequence stratigraphic architecture of the Northern Carnarvon Basin. *The APPEA Journal*, *56*, 143–158. <https://doi.org/10.1071/AJ15012>
- Gawthorpe, R. L., Andrews, J. E., Collier, R. E. L., Ford, M., Henstra, G. A., Kranis, H., ... Skourtos, E. (2017). Building up or out? Disparate sequence architectures along an active rift margin—Corinth rift, Greece. *Geology*, *45*(12), 1111–1114. <https://doi.org/10.1130/G39660.1>
- Gawthorpe, R. L., Fraser, A. J., & Collier, R. E. L. (1994). Sequence stratigraphy in active extensional basins: Implications for the interpretation of ancient basin-fills. *Marine and Petroleum Geology*, *11*, 642–658. [https://doi.org/10.1016/0264-8172\(94\)90021-3](https://doi.org/10.1016/0264-8172(94)90021-3)
- Gawthorpe, R. L., Hardy, S., & Ritchie, B. (2003). Numerical modelling of depositional sequences in half graben rift basins. *Sedimentology*, *50*, 169–185. <https://doi.org/10.1046/j.1365-3091.2003.00543.x>
- Gawthorpe, R. L., & Hurst, J. M. (1993). Transfer zones in extensional basins: Their structural style and influence on drainage development and stratigraphy. *Journal of the Geological Society, London*, *150*, 1137–1152. <https://doi.org/10.1144/gsjgs.150.6.1137>
- Gawthorpe, R. L., & Leeder, M. R. (2000). Tectono-sedimentary evolution of active extensional basins. *Basin Research*, *12*, 195–218. <https://doi.org/10.1046/j.1365-2117.2000.00121.x>
- Ghinassi, M. (2007). The effects of differential subsidence and coastal topography on high-order transgressive-regressive cycles: Pliocene nearshore deposits of the Val d'Orcia Basin, Northern Apennines,

- Italy. *Sedimentary Geology*, 202, 677–701. <https://doi.org/10.1016/j.sedgeo.2007.08.002>
- Gibbons, A. D., Barckhausen, U., Van Den Bogaard, P., Hoernle, K., Werner, R., Whittaker, J. M., & Müller, R. D. (2012). Constraining the Jurassic extent of Greater India: Tectonic evolution of the West Australian margin. *Geochemistry, Geophysics, Geosystems*, 13, 1–25. <https://doi.org/10.1029/2011GC003919>
- Gobo, K., Ghinassi, M., & Nemeč, W. (2015). Gilbert-type deltas recording short-term base-level changes: Delta-brink morphodynamics and related foreset facies. *Sedimentology*, 62, 1923–1949. <https://doi.org/10.1111/sed.12212>
- Gupta, S., Underhill, J. R., Sharp, I. R., & Gawthorpe, R. L. (1999). Role of fault interaction in controlling synrift dispersal patterns: Miocene, Abu Alaqa Group, Suez Rift, Sinai, Egypt. *Basin Research*, 11, 167–189.
- Hampson, G. J., Duller, R. A., Petter, A. L., Robinson, R. A. J., & Allen, P. A. (2014). Mass-balance constraints on stratigraphic interpretation of linked alluvial-coastal-shelfal deposits from source to sink: Example from Cretaceous Western Interior Basin, Utah and Colorado, USA. *Journal of Sedimentary Research*, 84, 935–960. <https://doi.org/10.2110/jrsr.2014.78>
- Hardy, S., & Gawthorpe, R. L. (1998). Effects of variations in fault slip rate on sequence stratigraphy in fan deltas: insights from numerical modeling. *Geology*, 26, 911–914.
- Hartley, R. A., Roberts, G. G., White, N., & Richardson, C. (2011). Transient convective uplift of an ancient buried landscape. *Nature Geoscience*, 4, 562–565. <https://doi.org/10.1038/ngeo1191>
- Heine, C., & Müller, R. (2005). Late Jurassic rifting along the Australian North West Shelf: Margin geometry and spreading ridge configuration. *Australian Journal of Earth Sciences*, 52, 27–39. <https://doi.org/10.1080/08120090500100077>
- Heldreich, G., Redfern, J., Legler, B., Gerdes, K., & Williams, B. P. J. (2017). Challenges in characterizing subsurface paralic reservoir geometries: a detailed case study of the Mungaroo Formation, North West Shelf, Australia. In G. J. Hampson, A. D. Reynolds, B. Kostic & M. R. Wells (Eds.), *Sedimentology of paralic reservoirs: recent advances*. Geological Society, London, *Special Publications*, 444, 59–108.
- Hengesh, J. V., & Whitney, B. B. (2016). Transcurrent reactivation of Australia's western passive margin: An example of intraplate deformation from the central Indo-Australian plate. *Tectonics*, 35, 1066–1089. <https://doi.org/10.1002/2015TC004103>
- Henstra, G. A., Gawthorpe, R. L., Helland-Hansen, W., Ravnås, R., & Rotevatn, A. (2017). Depositional systems in multiphase rifts: Seismic case study from the Lofoten margin, Norway. *Basin Research*, 29, 447–469. <https://doi.org/10.1111/bre.12183>
- Henstra, G. A., Grundvåg, S.-A., Johannessen, E. P., Kristensen, T. B., Midtkandal, I., Nystuen, J. P., ... Windelstad, J. (2016). Depositional processes and stratigraphic architecture within a coarse-grained rift-margin turbidite system: The Wollaston Forland Group, East Greenland. *Marine and Petroleum Geology*, 76, 187–209. <https://doi.org/10.1016/j.marpetgeo.2016.05.018>
- Hocking, R. M., Moors, H. T., & Van de Graaff, W. J. E. (1988). Regional Geology of the Northern Carnarvon Basin. In P. G. Purcell and R. R. Purcell (Eds.), *The North West Shelf, Australia*. Proceedings of Petroleum Exploration Society of Australia Symposium. PESA, Perth, 97–114.
- Hunt, D., & Gawthorpe, R. L. (2000). Sedimentary responses to forced regressions. *Geological Society, London, Special Publications*, 172, <https://doi.org/10.1144/GSL.SP.2000.172>
- Jackson, C.-A.-L., Gawthorpe, R. L., Carr, I. D., & Sharp, I. R. (2005). Normal faulting as a control on the stratigraphic development of shallow marine syn-rift sequences: The Nukhul and Lower Rudeis Formations, Hammam Faraun fault block, Suez Rift. *Egypt. Sedimentology*, 52, 313–338. <https://doi.org/10.1111/j.1365-3091.2005.00699.x>
- Jackson, C.-A.-L., Gawthorpe, R. L., & Sharp, I. R. (2006). Style and sequence of deformation during extensional fault-propagation folding: Examples from the Hammam Faraun and El-Qaa fault blocks, Suez Rift. *Egypt. Basin Research*, 28, 519–535.
- Jackson, C.-A.-L., Larsen, E., Hanslien, S., & Tjemsland, A.-E. (2011). Controls on synrift turbidite deposition on the hanging wall of the South Viking Graben, North Sea rift system, offshore Norway. *AAPG Bulletin*, 95, 1557–1587. <https://doi.org/10.1306/01031110037>
- Jackson, J. A., & Leeder, M. R. (1993). Drainage systems and the evolution of normal faults: An example from Pleasant Valley, Nevada. *Journal of Structural Geology*, 16, 1041–1059.
- Kallweit, R. S., & Wood, L. C. (1982). The limits of resolution of zero-phase wavelets. *Geophysics*, 47, 1035–1046. <https://doi.org/10.1190/1.1441367>
- Keep, M., Powell, C. M., & Baillie, P. W. (1998). Neogene deformation of the North West Shelf, Australia. In P. G. Purcell & R. R. Purcell (Eds.), *The Sedimentary Basins of Western Australia 2: Proceedings of Petroleum Exploration Society Australia Symposium* (pp. 81–91). Perth: PESA.
- L'Anson, A., Elders, C., & McHarg, S. (2019). Marginal fault systems of the northern Carnarvon Basin: Evidence for multiple Palaeozoic extension events, North- West Shelf, Australia. *Marine and Petroleum Geology*, 101, 211–229. <https://doi.org/10.1016/j.marpetgeo.2018.11.040>
- Leeder, M. R., Collier, R. E. L., Abdul Aziz, L. H., Trout, M., Ferentinos, G., Papatheodorou, G., & Lyberis, E. (2002). Tectono-sedimentary processes along an active marine/lacustrine half-graben margin: Alkyonides Gulf, E. Gulf of Corinth, Greece. *Basin Research*, 14, 25–41. <https://doi.org/10.1046/j.1365-2117.2002.00164.x>
- Leeder, M. R., & Gawthorpe, R. L. (1987). Sedimentary models for extensional tilt-block/half-graben basins. In M. P. Coward, J. F. Dewey & P. L. Hancock (Eds.), *Continental Extensional Tectonics*. Geological Society, London, *Special Publications*, 28, 139–152.
- Leeder, M. R., & Jackson, J. A. (1993). The interaction between normal faulting and drainage in active extensional basins, with examples from the western United States and central Greece. *Basin Research*, 5, 79–102. <https://doi.org/10.1111/j.1365-2117.1993.tb00059.x>
- Leeder, M. R., Mack, G. H., & Salyards, S. L. (1996). Axial-transverse fluvial interactions in half graben: Plio-Pleistocene Palomas Basin, southern Rio Grande Rift, New Mexico, USA. *Basin Research*, 8, 225–241. <https://doi.org/10.1046/j.1365-2117.1996.00192.x>
- Leppard, C. W., & Gawthorpe, R. L. (2006). Sedimentology of rift climax deep water systems; Lower Rudeis Formation, Hammam Faraun Fault Block, Suez Rift, Egypt. *Sedimentary Geology*, 191, 67–87. <https://doi.org/10.1016/j.sedgeo.2006.01.006>
- Lewis, M. M., Jackson, C.-A.-L., & Gawthorpe, R. L. (2015). Tectono-sedimentary development of early syn-rift deposits: The Abura Graben, Suez Rift. *Basin Research*, 29, 327–351.
- Lin, W., & Bhattacharya, J. P. (2017). Estimation of source-to-sink mass balance by a fulcrum approach using channel paleohydrologic parameters of the Cretaceous Dunvegan Formation, Canada. *Journal of Sedimentary Research*, 87, 97–116. <https://doi.org/10.2110/jrsr.2017.1>
- Longley, I. M., Buessenschuett, C., Clydsdale, L., Cubitt, C. J., Davis, R. C., Johnson, M. K., ... Thompson, N. B. (2002). The North West

- Shelf of Australia – a Woodside perspective. In M. Keep & S. J. Moss (Eds.), *The Sedimentary Basins of Western Australia 3: Proceedings of the Petroleum Society of Australia Symposium* (966). Perth: PESA.
- Marshall, N. G., & Lang, S. C. (2013). A New Sequence Stratigraphic Framework for the North West Shelf, Australia. In M. Keep & S. J. Moss (Eds.), *The Sedimentary Basins of Western Australia 4: Proceedings of Petroleum Exploration Society of Australia Symposium* (pp. 18–21). Perth: PESA.
- McArthur, A. D., Hartley, A. J., Archer, S. G., Jolley, D. W., & Lawrence, H. M. (2016). Spatiotemporal relationships of deep-marine, axial, and transverse depositional systems from the synrift Upper Jurassic of the central North Sea. *AAPG Bulletin*, *100*, 1469–1500. <https://doi.org/10.1306/04041615125>
- McArthur, A. D., Jolley, D. W., Hartley, A. J., Archer, S. G., & Lawrence, H. M. (2016). Palaeoecology of syn-rift topography: A Late Jurassic footwall island on the Josephine Ridge, Central Graben, North Sea. *Palaeogeography, Palaeoclimatology, Palaeoecology*, *459*, 63–75. <https://doi.org/10.1016/j.palaeo.2016.06.033>
- McHarg, S., Elders, C., & Cunneen, J. (2018). Normal fault linkage and reactivation, Dampier Sub-basin, Western Australia. *Australian Journal of Earth Science*, *66*, 209–225. <https://doi.org/10.1080/08120099.2019.1519848>
- McLeod, A. E., & Underhill, J. R. (1999). Processes and products of footwall degradation, northern Brent Field, Northern North Sea. *Geological Society, London, Petroleum Geology Conference Series*, *5*, 91–106. <https://doi.org/10.1144/0050091>
- McNeill, L. C., Cotterill, C. J., Henstock, T. J., Bull, J. M., Stefatos, A., Collier, R. E. L., ... Hicks, S. E. (2005). Active faulting within the offshore western Gulf of Corinth, Greece: Implications for models of continental rift deformation. *Geology*, *33*, 241–244. <https://doi.org/10.1130/G21127.1>
- Metcalfe, I. (1999). Gondwana dispersion and Asian accretion: An overview. In I. Metcalfe (Ed.), *Gondwana Dispersion and Asian Accretion – IGCP 321 Final Results Volume* (pp. 9–28). Rotterdam: A.A. Balkema.
- Michael, N. A., Whittaker, A. C., & Allen, P. A. (2013). The functioning of sediment routing systems using a mass balance approach: Example from the Eocene of the Southern Pyrenees. *The Journal of Geology*, *121*, 581–606. <https://doi.org/10.1086/673176>
- Mohrig, D., Heller, P. L., Paola, C., & Lyons, W. J. (2000). Interpreting avulsion process from ancient alluvial sequences: Guadalope-Matarranya (northern Spain) and Wasatch Formation (western Colorado). *Geological Society of America Bulletin*, *112*, 1787–1803.
- Monro, J. (2012). *Genseric-1 final well completion report, WA-434-P, Woodside*.
- Morley, C. K., Ionnikoff, Y., Pinyochon, N., & Seusutthiya, K. (2007). Degradation of a footwall fault block with hanging-wall fault propagation in a continental lacustrine setting: How a new structural model impacted field development plans, the Sirikit field, Thailand. *AAPG Bulletin*, *91*, 1637–1661. <https://doi.org/10.1306/06280707014>
- Mortimer, E. J., & Carrapa, B. (2007). Footwall drainage evolution and scarp retreat in response to increasing fault displacement: Loreto fault, Baja California Sur, Mexico. *Geology*, *35*, 651–654. <https://doi.org/10.1130/G23690A.1>
- Muravchik, M., Gawthorpe, R. L., Sharp, I. R., Rarity, F., & Hodgetts, D. (2018). Sedimentary environment evolution in a marine hanging-wall dip slope setting. El Qaa Fault Block, Suez Rift. *Egypt. Basin Research*, *30*, 452–478. <https://doi.org/10.1111/bre.12231>
- Nøttvedt, A., Berge, A. M., Dawers, N. H., Færseth, R. B., Häger, K. O., Mangerud, G., & Puigdefabregas, C. (2000). Syn-rift evolution and resulting play models in the Snorre-H area, northern North Sea. In A. Nøttvedt (Ed.), *Dynamics of the Norwegian Margin. Geological Society, London, Special Publications*, *167*, 179–218.
- Nyberg, B., Helland-Hansen, W., Gawthorpe, R. L., Sandbakken, P. H., Eide, C., Sømme, T., ... Leiknes, S. (2018). Revisiting morphological relationships of modern source-to-sink segments as a first-order approach to scale ancient sedimentary systems. *Sedimentary Geology*, *373*, 111–133. <https://doi.org/10.1016/j.sedgeo.2018.06.007>
- Olariu, C., & Bhattacharya, J. P. (2006). Terminal distributary channels and delta front architecture of river-dominated delta systems. *Journal of Sedimentary Research*, *76*, 212–233. <https://doi.org/10.2110/jsr.2006.026>
- Ortiz-Karpf, A., Hodgson, D. M., & McCaffrey, W. D. (2015). The role of mass-transport complexes in controlling channel avulsion and the subsequent sediment dispersal patterns on an active margin: The Magdalena Fan, offshore Colombia. *Marine and Petroleum Geology*, *6*, 58–75. <https://doi.org/10.1016/j.marpetgeo.2015.01.005>
- Paola, C., & Martin, J. M. (2012). Mass-balance effects in depositional systems. *Journal of Sedimentary Research*, *82*, 435–450. <https://doi.org/10.2110/jsr.2012.38>
- Papadopoulos, G., & Pavlides, S. (1992). The large 1956 earthquake in the South Aegean: Macro seismic field configuration, faulting and neotectonics of Amorgos Island. *Earth Planet. Sci. Letters*, *113*, 383–396. [https://doi.org/10.1016/0012-821X\(92\)90140-Q](https://doi.org/10.1016/0012-821X(92)90140-Q)
- Pechlivanidou, S., Cowie, P. A., Hannisdal, B., Whittaker, A. C., Gawthorpe, R. L., Pennos, C., & Riiser, O. S. (2018). Source-to-sink analysis in an active extensional setting: Holocene erosion and deposition in the Sperchios rift, central Greece. *Basin Research*, *30*, 522–543. <https://doi.org/10.1111/bre.12263>
- Phillips Australian Oil Company (1980). Jupiter-1 well completion report, WA-84-P. Australian Government Geoscience Australia.
- Prélat, A., Hodgson, D. M., & Flint, S. S. (2009). Evolution, architecture and hierarchy of distributary deep-water deposits: A high-resolution outcrop investigation from the Permian Karoo Basin, South Africa. *Sedimentology*, *56*, 2132–2154. <https://doi.org/10.1111/j.1365-3091.2009.01073.x>
- Ravnås, R., & Steel, R. J. (1998). Architecture of Marine Rift-Basin Successions. *AAPG Bulletin*, *82*, 110–146.
- Reading, H. G., & Richards, M. (1994). Turbidite systems in deep-water basin margins classified by grain size and feeder system. *AAPG Bulletin*, *78*, 792–822.
- Richards, M., Bowman, M., & Reading, H. (1998). Submarine fan systems characterization and stratigraphic prediction. *Marine and Petroleum Geology*, *15*, 689–717.
- Roberts, A. M., Kuszniir, N. J., Yielding, G., & Beeley, H. (2019). Mapping the bathymetric evolution of the Northern North Sea: From Jurassic synrift archipelago through Cretaceous-Tertiary post-rift subsidence. *Petroleum Geoscience*, *25*, 306–321. <https://doi.org/10.1144/petgeo2018-066>
- Roberts, A. M., Yielding, G., & Badley, M. E. (1993). Tectonic and bathymetric controls on stratigraphic sequences within evolving half-graben. In G. D. Woudiamis & A. Dobb (Eds.), *Tectonics and seismic sequence stratigraphy. Geological Society Special Publication*, *71*, 87–121.
- Rohais, S., Eschard, R., & Guillocheau, F. (2008). Depositional model and stratigraphic architecture of rift climax Gilbert-type fan deltas (Gulf of Corinth, Greece). *Sedimentary Geology*, *210*, 132–145. <https://doi.org/10.1016/j.sedgeo.2008.08.001>

- Serck, C. S., & Braathen, A. (2019). Extensional fault and fold growth: Impact on accommodation evolution and sedimentary infill. *Basin Research*, 31(5), 967–990. <https://doi.org/10.1111/bre.12353>
- Sharp, I. R., Gawthorpe, R. L., Armstrong, B., & Underhill, J. R. (2000). Propagation history and passive rotation of mesoscale normal faults: Implications for synrift stratigraphic development. *Basin Research*, 12, 285–305. <https://doi.org/10.1046/j.1365-2117.2000.00132.x>
- Sharp, I. R., Gawthorpe, R. L., Underhill, J. R., & Gupta, S. (2000). Fault-propagation folding in extensional settings: Examples of structural style and synrift sedimentary response from the Suez rift, Sinai, Egypt. *Geological Society of America Bulletin*, 112, 1877–1899. [https://doi.org/10.1130/0016-7606\(2000\)112<1877:FPFIES>2.0.CO;2](https://doi.org/10.1130/0016-7606(2000)112<1877:FPFIES>2.0.CO;2)
- Smallwood, J. R., & Gill, C. E. (2002). The rise and fall of the Faroe-Shetland Basin: Evidence from seismic mapping of the Balder Formation. *Journal of the Geological Society*, 159, 627–630. <https://doi.org/10.1144/0016-764902-064>
- Stagg, H. M. J., & Colwell, J. B. (1994). The structural foundations of the Northern Carnarvon Basin. In: P. G. Purcell & R. R. Purcell (Eds.), *The North West Shelf, Australia. Proceedings of Petroleum Exploration Society of Australia Symposium* (pp. 349–372). Perth: PESA.
- Stevenson, C. J., Jackson, C.-A.-L., Hodgson, D. M., Hubbard, S. M., & Eggenhuisen, J. T. (2015). Deep-water sediment bypass. *Journal of Sedimentary Research*, 85, 1058–1081. <https://doi.org/10.2110/jsr.2015.63>
- Steventon, M., Jackson, C.-A.-L., Hodgson, D. M., & Johnson, H. D. (2019). Lateral variability of shelf-edge, slope and basin-floor deposits. Santos Basin, Brazil. <https://doi.org/10.31223/osf.io/eagqd>
- Stewart, S. A., & Reeds, A. (2003). Geomorphology of kilometre-scale extensional fault scarps: Factors that impact seismic interpretation. *AAPG Bulletin*, 87, 251–272.
- Stiros, S. C., Marangou, L., & Arnold, M. (1994). Quaternary uplift and tilting of Amorgos Island (southern Aegean) and the 1956 earthquake. *Earth and Planetary Science Letters*, 128, 65–76. [https://doi.org/10.1016/0012-821X\(94\)90135-X](https://doi.org/10.1016/0012-821X(94)90135-X)
- Straub, K. M., & Pyles, D. R. (2012). Quantifying the hierarchical organization of compensation in submarine fans using surface statistics. *Journal of Sedimentary Research*, 82, 889–898. <https://doi.org/10.2110/jsr.2012.73>
- Stucky de Quay, G., Roberts, G. G., Watson, J. S., & Jackson, C.-A.-L. (2017). Incipient mantle plume evolution: Constraints from ancient landscapes buried beneath the North Sea. *Geochemistry, Geophysics, Geosystems*, 18, 973–993. <https://doi.org/10.1002/2016GC006769>
- Sturrock, V. (2011). *Dalia South-1 well completion report, interpretive volume, WA-348-P*. Woodside.
- Taylor, L. (2008). *Belicoso-1 final well completion report, interpretive volume, WA-347-P*. Woodside.
- Taylor, L. (2012). *Cadwallon-1 final well completion report, interpretive volume, WA-434-P*. Woodside.
- Tindale, K., Newell, N., Keall, J., & Smith, N. (1998). Structural evolution and charge history of the Exmouth Sub-basin, northern Carnarvon Basin, western Australia. In: P. G. Purcell & R. R. Purcell (Eds.), *The Sedimentary Basins of Western Australia 2: Proceedings of the Petroleum Exploration Society of Australia*. PESA, Perth, 447–472.
- Turner, C. C. & Cronin, B. T. (Eds.). (2018). Rift-related coarse-grained submarine fan reservoirs; the Brae Play, South Viking Graben, North Sea. *AAPG Memoir*, 115, 630.
- Underhill, J. R., Sawyer, M. J., Hodgson, P., Shallcross, M. D., & Gawthorpe, R. L. (1997). Implications of fault scarp degradation for Brent Group prospectivity, Ninian Field, northern North Sea. *AAPG Bulletin*, 81, 999–1022.
- Veevers, J. J. (1988). Morphotectonics of Australia's northwestern margin – a review. In: P. G. Purcell & R. R. Purcell (Eds.), *The North West Shelf, Australia: Proceedings of Petroleum Exploration Society of Australia Symposium*. PESA, Perth, 651.
- Walsh, J. J., & Watterson, J. (1988). Analysis of the relationship between displacements and dimensions of faults. *Journal of Structural Geology*, 10, 239–247. [https://doi.org/10.1016/0191-8141\(88\)90057-0](https://doi.org/10.1016/0191-8141(88)90057-0)
- Wang, Y., Straub, K. M., & Hajek, E. A. (2011). Scale-dependent compensational stacking: An estimate of autogenic time scales in channelized sedimentary deposits. *Geology*, 39, 811–814. <https://doi.org/10.1130/G32068.1>
- Watkins, S. E., Whittaker, A. C., Bell, R. E., McNeill, L. C., Gawthorpe, R. L., Brooke, S. A. S., & Nixon, C. W. (2018). Are landscapes buffered to high-frequency climate change? A comparison of sediment fluxes and depositional volumes in the Corinth Rift, central Greece, over the past 130 k.y. *GSA Bulletin*, 131, 372–388. <https://doi.org/10.1130/B31953.1>
- Welbon, A. I. F., Brockbank, P. J., Brunnsden, D., & Olsen, T. S. (2007). Characterizing and producing from reservoirs in landslides: challenges and opportunities. In: S. J. Jolley, D. Barr, J. J. Walsh & R. J. Knipe (Eds.), *Structurally Complex Reservoirs. Geological Society, London, Special Publications*, 292, 49–74. <https://doi.org/10.1144/SP292.3>
- Whittaker, A. C., Attal, M., & Allen, P. A. (2010). Characterising the origin, nature and fate of sediment exported from catchments perturbed by active tectonics. *Basin Research*, 22, 809–828.
- Widess, M. B. (1973). How thin is a thin bed? *Geophysics*, 38, 1176–1180. <https://doi.org/10.1190/1.1440403>
- Williams, R. M. (2018). Derisking the Thebe Discovery through cognitive interpretation. *First Break*, 36, 71–78.
- Yeates, A. N., Bradshaw, M. T., & Dickins, J. M. (1987). The Westralian Superbasin: an Australian link with Tethys. In K. G. McKenzie (Ed.), *Shallow Tethys* (Vol. 2, pp. 199–213). Rotterdam, Netherlands: A. A. Balkema. 199–213.
- Yielding, G., Badley, M. E., & Roberts, A. M. (1992). The structural evolution of the Brent Province. *Geological Society, London, Special Publications*, 61, 27–43. <https://doi.org/10.1144/GSL.SP.1992.061.01.04>
- Young, M. J., Gawthorpe, R. L., & Sharp, I. R. (2002). Architecture and evolution of syn-rift clastic depositional systems towards the tip of a major fault segment, Suez Rift, Egypt. *Basin Research*, 14(1), 23. <https://doi.org/10.1046/j.1365-2117.2002.00162.x>

SUPPORTING INFORMATION

Additional Supporting Information may be found online in the Supporting Information section.

How to cite this article: Barrett BJ, Hodgson DM, Jackson CA-L, Lloyd C, Casagrande J, Collier REL. Quantitative analysis of a footwall-scarp degradation complex and syn-rift stratigraphic architecture, Exmouth Plateau, NW Shelf, offshore Australia. *Basin Res.* 2020;00:1–35. <https://doi.org/10.1111/bre.12508>